



Cluster-based density-functional approach to quantum transport through molecular and atomic contacts

To cite this article: F Pauly *et al* 2008 *New J. Phys.* **10** 125019

View the [article online](#) for updates and enhancements.

Related content

- [Heat dissipation and its relation to thermopower in single-molecule junctions](#)
L A Zotti, M Bürkle, F Pauly *et al.*
- [Atomistic theory of transport](#)
Alessandro Pecchia and Aldo Di Carlo
- [O\(N\) methods in electronic structure calculations](#)
D R Bowler and T Miyazaki

Recent citations

- [Effect of Charge Assisted Hydrogen Bonds on Single Molecule Electron Transport](#)
Valentina Sacchetti *et al*
- [Electric-Field-Controllable Conductance Switching of an Overcrowded Ethylene Self-Assembled Monolayer](#)
Shintaro Fujii *et al*
- [Thermal conductance of single-molecule junctions](#)
Longji Cui *et al*

Cluster-based density-functional approach to quantum transport through molecular and atomic contacts

F Pauly^{1,2,7}, J K Viljas^{1,2}, U Huniar^{3,4}, M Häfner¹,
S Wohlthat^{1,5}, M Bürkle¹, J C Cuevas^{1,2,6}
and G Schön^{1,2}

¹ Institut für Theoretische Festkörperphysik and DFG-Center for Functional Nanostructures, Universität Karlsruhe, 76128 Karlsruhe, Germany

² Institut für Nanotechnologie, Forschungszentrum Karlsruhe, 76021 Karlsruhe, Germany

³ COSMOlogic GmbH and Co KG, Burscheider Street 515, 51381 Leverkusen, Germany

⁴ Institut für Physikalische Chemie, Universität Karlsruhe, 76128 Karlsruhe, Germany

⁵ School of Chemistry, The University of Sydney, Sydney, NSW 2006, Australia

⁶ Departamento de Física Teórica de la Materia Condensada, Universidad Autónoma de Madrid, 28049 Madrid, Spain

E-mail: fabian.pauly@kit.edu

New Journal of Physics **10** (2008) 125019 (28pp)

Received 25 June 2008

Published 4 December 2008

Online at <http://www.njp.org/>

doi:10.1088/1367-2630/10/12/125019

Abstract. We present a cluster-based approach to model charge transport through molecular and atomic contacts. The electronic structure of the contacts is determined in the framework of density functional theory, and the parameters needed to describe transport are extracted from finite clusters. A similar procedure, restricted to nearest-neighbor interactions in the electrodes, has been presented by Damle *et al* (2002 *Chem. Phys.* **281** 171). Here, we show how to systematically improve the description of the electrodes by extracting bulk parameters from sufficiently large metal clusters. In this way, we avoid problems

⁷ Author to whom any correspondence should be addressed.

arising from the use of nonorthogonal basis functions. For demonstration, we apply our method to electron transport through Au contacts with various atomic-chain configurations and to a single-atom contact of Al.

Contents

1. Introduction	2
2. Theoretical approach	4
2.1. Electronic structure	4
2.2. Transport formalism	4
2.3. Implementation of the transport method	6
3. Metallic atomic contacts	8
3.1. Gold contacts	8
3.2. Aluminium contacts	13
4. Conclusions	14
Acknowledgments	15
Appendix A. Nonorthogonal, local basis sets	15
Appendix B. Bulk parameters from finite clusters	17
Appendix C. Electrode Green's functions	22
References	26

1. Introduction

Advances in the experimental techniques for manipulating atomic-sized objects have turned the vision of molecular-scale electronic circuits into a realistic goal [1]–[5]. This has intensified the interdisciplinary efforts to study charge transport in nanostructures. Ideally, the circuits would be constructed in a bottom-up fashion with functional units and all the wiring on the molecular scale. To approach this goal, present-day experiments in the area of molecular electronics concentrate on measuring the current–voltage response of single molecules contacted to metallic electrodes. In these studies, also purely metallic atomic contacts serve as important reference systems [6].

In order to support the experiments and to stimulate further technological advance, theoretical modeling of charge transport at the atomic scale is needed. Here, one faces the challenge to describe infinitely extended, low-symmetry quantum systems that may, in addition, be far from equilibrium and involve strong electronic correlations. While a complete theoretical understanding is still lacking, sophisticated *ab initio* methods have been developed for approximate but parameter-free numerical simulations. In order to study the prototypical metal–molecule–metal systems or metallic atomic contacts, many groups employ density functional theory (DFT) combined with nonequilibrium Green's function (NEGF) techniques [7]–[22]. Some shortcomings related to the use of DFT in this context have been pointed out, and solutions are being sought [23]–[26]. On the other hand, DFT presently appears to be one of the few practicable *ab initio* electronic structure methods, since studies of quantum transport require dealing with a large number of atoms. Furthermore, it can handle the hybrid metal–molecule–metal contacts, where the central regions, comprising the molecule, are frequently rather insulator-like, whereas the electrodes are metallic. For a more complete discussion, we refer to [27]–[29].

The DFT approaches can mainly be divided into two types. In the first type, atomic-sized contacts are modeled by periodically repeated supercells, and computer codes developed for solid-state calculations are employed [7, 15, 22]. The use of periodic boundary conditions facilitates the electrode description. However, typically the conductance is determined for an array of parallel junctions and may be affected by artificial interactions between them. The second type is based on finite clusters and originates more from the chemistry community [8, 9, 14, 16, 21]. It has the advantage that genuinely single-atom or single-molecule contacts are studied. The drawback is commonly the description of the electrodes, since it is difficult to treat bulk properties based on finite clusters. Furthermore, the coupling between the central region and the electrodes can be complicated by finite-size and surface mismatch effects.

To arrive at an *ab initio* DFT description it is desirable to treat the whole system consistently by using the same basis set and exchange-correlation functional everywhere. The problem of the cluster-based approaches regarding the electrodes is apparent, for example, from the work of [8, 9, 21], where the authors resort to a separate tight-binding parametrization obtained from the literature [30]. In such cases, uncertainties mainly arise from the coupling between the central region and the electrodes, which requires knowledge about level alignments and basis functions. Damle *et al* proposed to resolve this issue by extracting bulk parameters from finite clusters computed within DFT [16, 31]. However, their treatment of the electrodes should be seen as a first approximation, since only couplings between nearest-neighbor atoms were considered. Furthermore, they finally use energy-independent self-energies, which is well justified only for electrode materials with a constant density of states (DOS) near the Fermi energy E_F .

In this work, we present a cluster-based DFT approach for the atomistic description of quantum transport. We follow the ideas of Damle *et al* [31], but place special emphasis on the treatment of the electrodes. In particular, we show that extracting bulk parameters from small metal clusters can lead to an unphysical behavior of the overlap of the nonorthogonal basis functions in k -space. The description of the electrodes can be improved systematically by employing metal clusters of increasing size. Our implementation is based on the quantum-chemistry package TURBOMOLE, which allows us to study clusters of several hundred atoms. In this way, we obtain an *ab initio* formulation of quantum transport in atomic-sized contacts, where the whole system is treated on an equal footing. It has the advantage that we can employ well-tested, high-quality quantum-chemical Gaussian basis sets. Since energies in our isolated systems are measured with respect to the vacuum level, we can directly compare values for E_F to experimental work functions⁸. Furthermore, our method offers a high degree of geometric flexibility. Thus, we can describe contact configurations with molecules of large transverse extent and with electrodes that are laterally offset or tilted relative to each other.

The theoretical framework of our approach is presented in section 2. Several technical details related to the use of nonorthogonal basis functions and the electrode treatment can be found in appendices A–C. To demonstrate the usefulness of our method, we study in section 3 the transport properties of atomic contacts of Au and Al. The choice of these materials is motivated by the fact that Au exhibits a rather energy independent DOS near E_F , whereas Al does not. Furthermore, for these systems, we can compare our results with the literature. We find good agreement, and demonstrate the sufficient robustness of our calculations. Further applications have been presented in [32]–[36]. We summarize our results in section 4.

⁸ Due to the missing surfaces, the same would not be possible if we had obtained the bulk parameters from calculations of a crystal using periodic boundary conditions [56].

2. Theoretical approach

2.1. Electronic structure

Our *ab initio* calculations are based on the implementation of DFT in TURBOMOLE 5.9 [37]. By *ab initio* we mean that the simulations require no system-specific parameters. Self-consistent DFT calculations of large systems are generally very time-consuming. TURBOMOLE, however, is specialized in handling such systems, and offers several possibilities to reduce the computational effort. Most essential are the techniques of the ‘resolution of the identity in J ’ (RI- J) [38, 39] and the ‘multipole-accelerated resolution of the identity J ’ (MARI- J) [40], which are both implemented in the *ridft* module of TURBOMOLE. The approximations help to reduce the effort to compute the Coulomb integrals J , which are particularly expensive to evaluate. With the help of the RI- J approximation, known also under the name ‘density fitting’, the four-center-two-electron integrals can be expressed as three-center-two-electron ones [41]. Calculations are faster by a factor of 10–100 as compared with standard DFT, but equally accurate. The MARI- J technique adds to RI- J an efficient treatment of Coulomb interactions between distant atoms. The interactions are divided into a near-field and a far-field part, where the near field is treated with RI- J and the far field by a multipole approximation. Compared with RI- J , it can accelerate the calculations by another factor of 2–7 [40]. Besides, if the contact configuration admits, one can exploit point group symmetries, including non-Abelian ones. In this way, the calculations speed up further by a factor given by the order of the point group.

DFT requires the choice of an exchange-correlation functional [42]. We select the generalized-gradient functional BP86 [43, 44], which is known to yield good results for large metal clusters [45]–[48]. Since it contains no contribution of Hartree–Fock exchange, it is efficiently evaluated within RI- J or MARI- J . To express the orbital wave functions, Gaussian basis sets of split-valence-polarization (SVP) quality are used [38, 39, 49], which are the TURBOMOLE standard. Within the closed-shell formalism of DFT, total energies of all our clusters are converged to a precision better than 10^{-6} au. In order to obtain ground-state structures, the total energy needs to be minimized with respect to the nuclear coordinates. We perform such geometry optimizations or ‘relaxations’ until the maximum norm of the Cartesian gradient has fallen below 10^{-4} au.

2.2. Transport formalism

We compute transport properties of atomic-sized contacts using the Landauer–Büttiker theory and Green’s functions expressed in a nonorthogonal basis of atomic-like orbitals [50, 51]. The local nature of the basis allows us to partition the basis states $|i, \alpha\rangle$ into left (L), central (C) and right (R) ones, according to a division of the contact geometry. In the basis states, α refers to the type of orbital at the position of atom i . For reasons of brevity, we will frequently suppress the orbital index. The Hamiltonian (or Kohn–Sham) matrix $H_{i\alpha,j\beta} = \langle i, \alpha | H | j, \beta \rangle$, and analogously the overlap matrix $S_{i\alpha,j\beta} = \langle i, \alpha | j, \beta \rangle$, can thus be written in block form,

$$H = \begin{pmatrix} H_{LL} & H_{LC} & 0 \\ H_{CL} & H_{CC} & H_{CR} \\ 0 & H_{RC} & H_{RR} \end{pmatrix}. \quad (1)$$

Both S and H are real-valued and are hence symmetric. In addition, we assume the C region to be large enough to have $S_{LR} = H_{LR} = 0$. Within the Landauer–Büttiker theory [52], the linear

conductance can be expressed as

$$G = \frac{2e^2}{h} \int dE \left[-\frac{\partial}{\partial E} f(E, T) \right] \tau(E), \quad (2)$$

where $f(E, T) = \{\exp[(E - \mu)/k_B T] + 1\}^{-1}$ is the Fermi function, and the chemical potential μ is approximately equal to E_F . Using the standard NEGF technique, the transmission function is given by

$$\tau(E) = \text{Tr} [\Gamma_L(E) G_{CC}^r(E) \Gamma_R(E) G_{CC}^a(E)] = \text{Tr} [t^\dagger(E) t(E)] \quad (3)$$

with the transmission matrix

$$t(E) = \sqrt{\Gamma_R(E)} G_{CC}^a(E) \sqrt{\Gamma_L(E)}. \quad (4)$$

Here, we define Green's functions

$$G_{CC}^r(E) = [E S_{CC} - H_{CC} - \Sigma_L^r(E) - \Sigma_R^r(E)]^{-1} \quad (5)$$

and $G_{CC}^a = [G_{CC}^r]^\dagger$, the self-energies

$$\Sigma_X^r(E) = (H_{CX} - E S_{CX}) g_{XX}^r(E) (H_{XC} - E S_{XC}) \quad (6)$$

and the hopping-rate matrices

$$\Gamma_X(E) = -2\text{Im} [\Sigma_X^r(E)], \quad (7)$$

where $g_{XX}^r = (E S_{XX} - H_{XX})^{-1}$ is the electrode Green's function for lead $X = L, R$. At low temperatures, the expression for the conductance simplifies to

$$G = \frac{2e^2}{h} \tau(E_F) = G_0 \sum_n \tau_n(E_F), \quad (8)$$

with $G_0 = 2e^2/h$ the quantum of conductance and τ_n the eigenvalues of $t^\dagger t$. The latter are the transmission probabilities of the transmission eigenchannels n .⁹ Also other observables, such as the thermopower or the photoconductance, can be studied based on the knowledge of $\tau(E)$ [32, 36, 53, 54].

Information on the position of energy levels of a system may help to identify conduction mechanisms. Such information can be extracted from the spectral density [48]

$$\rho(E) = \frac{i}{2\pi} [G^r(E) - G^a(E)] = -\frac{1}{\pi} \text{Im} [G^r(E)]. \quad (9)$$

Using this, we define the local density of states (LDOS) at atom i and its decomposition into orbitals α via

$$\text{LDOS}_i(E) = \sum_\alpha \text{LDOS}_{i\alpha}(E), \quad (10)$$

$$\text{LDOS}_{i\alpha}(E) = \left(S_{CC}^{1/2} \varrho_{CC}(E) S_{CC}^{1/2} \right)_{i\alpha, i\alpha}. \quad (11)$$

In appendix A, we discuss the approximations involved in this definition. There, we also consider further the issues related to the use of nonorthogonal basis sets to evaluate the single-particle Green's functions and the electric current.

⁹ The fact that the τ_n are probabilities, i.e. that $0 \leq \tau_n \leq 1$, can be proven by defining $r = 1 + i\sqrt{\Gamma_L} G_{CC}^a \sqrt{\Gamma_L}$ such that $r^\dagger r + t^\dagger t = 1$. Using relations presented in appendix A.3, it is easy to show the positive-semidefiniteness of Γ_L , necessary for the determination of both r and t (equation (4)).

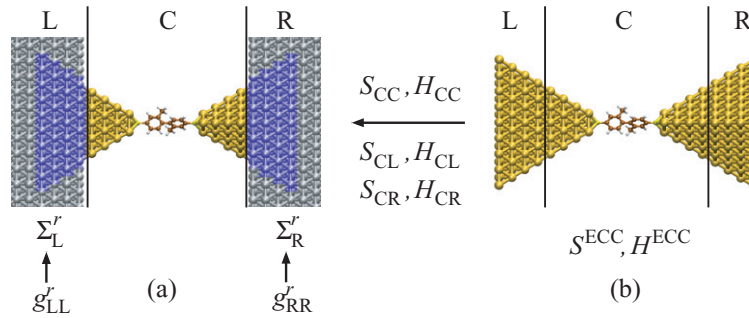


Figure 1. Quantum transport scheme. The atomic-sized contact (a) is divided into a C region and two semi-infinite L and R electrodes. Using a similar division for the ECC (b), information on the electronic structure of the C region (S_{CC} , H_{CC}) as well as the CL and CR couplings (S_{CL} , H_{CL} and S_{CR} , H_{CR}) is extracted. In order to obtain the self-energies Σ_L^r and Σ_R^r , the remaining task is to determine the electrode surface Green's functions g_{LL}^r and g_{RR}^r . This procedure is described further below in the text.

2.3. Implementation of the transport method

2.3.1. Central system. In order to determine the transmission function $\tau(E)$, we need a practical scheme to obtain the necessary information on the electronic structure. In figure 1, we present our procedure. The goal is to describe the whole atomic-sized contact (figure 1(a)) consistently, by treating the L, C and R regions with the same basis set and exchange-correlation functional. We obtain the parameters S_{CC} and H_{CC} as well as the couplings to the electrodes S_{CX} and H_{CX} with $X = L, R$ from the extended central system (ECC) (figure 1(b)), in which we include large parts of the tips of the metallic electrodes. The division of the ECC into the L, C and R regions is performed so that the C region is identical to that in figure 1(a). The atoms in the L and R parts of the ECC (blue-shaded regions in figure 1(a)) correspond to that part of the electrodes, which is assumed to couple to C. The partitioning of the ECC is commonly made somewhere in the middle of the metal tips, and we will also refer to it as ‘cut’. The electrodes (L and R regions in figure 1(a)) are modeled as surfaces of semi-infinite crystals, described by the surface Green's functions g_{XX}^r . They are constructed from bulk parameters, extracted from large metal clusters. Let us now discuss how this is accomplished.

2.3.2. Electrodes. We extract bulk parameters describing perfect crystals from large metal clusters. The complete procedure, which aims at determining the surface Green's functions g_{XX}^r with $X = L, R$ is summarized in figure 2. In this work, we study exclusively electrode materials with an fcc structure, of which Au and Al are examples.

In a first step (figure 2(a)), we construct spherical metal clusters, henceforth called ‘spheres’. They are made up of atoms at positions $\{\vec{R}_j | \vec{R}_j = \sum_{n=1}^3 j_n \vec{a}_n \wedge |\vec{R}_j| \leq R^{\text{sphere}}\}$ with the standard primitive vectors \vec{a}_n of the fcc lattice and the sphere radius R^{sphere} . We will generally use the vector of integer indices $j = (j_1, j_2, j_3)$ to characterize the atomic position \vec{R}_j . We do not optimize the geometry of the spheres, but set the lattice constant a_0 to its experimental literature value [56]. Increasing the radius R^{sphere} should make the electronic structure in the center resemble that of a crystal. From the clusters we extract the overlap and Hamiltonian between the central atom at position 0 and the neighboring ones at position j (including $j = 0$).

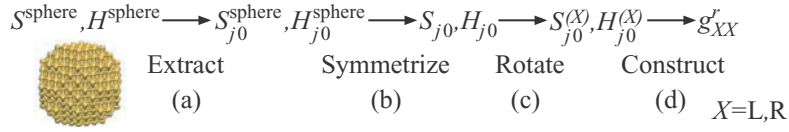


Figure 2. In order to obtain the electrode Green's functions g'_{XX} for lead $X = L, R$, we determine bulk parameters from large metal clusters. In a first step (a) we extract overlap and hopping elements, $S_{j0}^{\text{sphere}}, H_{j0}^{\text{sphere}}$, from the cluster's central atom to all its neighbors. They are (b) symmetrized by imposing the space group of the electrode lattice. After (c) a rotation to adapt them to the orientation of the respective electrode, (d) g'_{XX} is constructed with the help of a decimation procedure.

This yields the matrix elements $S_{j\alpha,0\beta}^{\text{sphere}}$ and $H_{j\alpha,0\beta}^{\text{sphere}}$, where α and β stand for the basis functions of the atoms at j and 0. For reasons of brevity, we will often suppress the orbital indices. S_{j0}^{sphere} and H_{j0}^{sphere} are then matrices with appropriate dimensions. The bulk parameters S_{j0}, H_{j0} need to satisfy the symmetries of the fcc space group (figure 2(b)). While S_{j0}^{sphere} depends only on the relative position of atoms, surface effects due to the finite size of the fcc clusters lead to deviations from the translational symmetry for H_{j0}^{sphere} . A rotation may still be necessary to arrive at parameters $S_{j0}^{(X)}, H_{j0}^{(X)}$, which are adapted to the orientation of the electrode $X = L, R$ (figure 2(c)). Details on the symmetrization procedure and the transformation of bulk parameters under rotations are presented in appendix B. The parameters $S_{j0}^{(X)}, H_{j0}^{(X)}$ are finally employed to construct the semi-infinite crystals and to obtain the surface Green's function g'_{XX} (figure 2(d)). Due to the finite range of the couplings S_{CX}, H_{CX} , we need to determine g'_{XX} for the first few surface layers only (blue-shaded regions in figure 1(a)). We compute these with the help of the decimation technique of [57], which we have generalized to deal with the nonorthogonal basis sets [58]. The complete procedure is explained in detail in appendix C. The parameters S_{j0}, H_{j0} can be computed once for a given metal and can then be used in transport calculations with electrodes of various spatial orientations.

For Au ($a_0 = 4.08 \text{ \AA}$), we have analyzed spheres ranging between 13 and 429 atoms, whereas for Al ($a_0 = 4.05 \text{ \AA}$) they vary between 13 and 555 atoms. Since we want to describe bulk, the parameters extracted from the largest clusters will obviously provide the best description. There is, however, an additional criterion, which necessitates the use of large metal clusters for a reliable description of the electrodes. As discussed in appendix B.1, it is based on the positive-semidefiniteness of the bulk overlap matrix. We find a strong violation of this criterion, if the extraction of parameters is performed such that only the couplings of the central atom to its nearest neighbors are considered. As a further demonstration of the quality of our description, we show in appendix B.2 the convergence of the DOS with respect to R^{sphere} .

For the transport calculations, we need a value for the Fermi energy. The biggest Au and Al spheres computed, Au₄₂₉ and Al₅₅₅, respectively, are very metallic. They exhibit differences between the highest occupied molecular orbital and the lowest unoccupied molecular orbital of less than 0.06 eV. Therefore, we set E_F halfway between these energies. In this way, we obtain $E_F = -5.0 \text{ eV}$ for Au and $E_F = -4.3 \text{ eV}$ for Al. The values will be used in all the results below. Notice that the negative values of E_F agree well with experimental work functions of 5.31–5.47 eV for Au and 4.06–4.26 eV for Al [59].

2.3.3. Discussion. In our approach, we assume the metal tips included in the ECC (figure 1(b)) to be large enough to satisfy basically two criteria. Firstly, all the charge transfer between the L and R electrodes and the C part of the contact should be accounted for. This ensures the proper alignment of the electronic levels in C with E_F . Secondly, most of the metal tips, especially the L and R parts of the ECC, should resemble bulk as closely as possible. Under these circumstances, the highest occupied molecular orbital of the ECC should be very similar to E_F , and we can evaluate the surface Green's functions by using bulk parameters of an infinitely extended crystal. Owing to the finite size of the cluster, the criteria can be satisfied only approximately. The mismatch between the parameters in the L and R regions of the contact and the ECC will thus lead to spurious scattering at the LC and CR interfaces. In principle this resistance can be eliminated systematically by including more atoms in the metal tips of the ECC. On the other hand, if the resistance in the C region is much larger than the spurious LC and CR interface resistances, they will have little influence on the results.

In order to describe the organic molecule in a single-molecule contact, it might be desirable to use a hybrid functional with a certain amount of Hartree–Fock exchange. However, the exchange interactions greatly increase the computational effort due to their nonlocal character, and may even lead to problems in the self-consistent iterations of DFT for rather metallic systems [60]. To treat the ECC and spherical metal cluster consistently, the exchange may be evaluated using a screened Coulomb potential [60]. A more approximate solution would be to mix two functionals, by including a portion of Hartree–Fock exchange for the ECC, but not for the sphere. In this way, the exchange would be taken into account, where it is most essential.

3. Metallic atomic contacts

In this section, we explore the conduction properties of metallic atomic contacts of Au and Al. These systems, in particular atomic-sized Au contacts, have been studied in detail both experimentally and theoretically, and can therefore be used to test our method. We start by discussing the transport properties of the Au contacts, consisting of a four-atom chain, a three-atom chain, and a two-atom chain or ‘dimer’. Since Al does not form chains of more than two atoms [61], we consider only a single-atom contact. Results for Al dimer contacts were already reported in [33]. For all systems, we analyze the transmission, its decomposition into eigenchannels, and, in order to obtain knowledge about the conduction mechanism, the LDOS for atoms in the narrowest part of the contact. Moreover, we investigate the robustness of our transmission curves with respect to different partitionings of the large ECCs.

3.1. Gold contacts

Let us first discuss the electronic structure of Au, where we display the DOS in figure 3. The Fermi energy at $E_F = -5.0$ eV is located in a fairly structureless, flat region somewhat above the d band. Based on the electronic configuration [Xe] $4f^{14} 5d^{10} 6s^1$ of the atom, one might have expected a strong contribution only from the s orbitals at E_F . But, as is visible from figure 3(b), s, p and d contributions are all comparable¹⁰. This signifies that valence orbitals hybridize strongly in the metal.

¹⁰ The orbital contributions are obtained by summing over all the basis functions of a certain angular symmetry: p_x , for example, results from a sum over all the p_x functions of the basis set, and p is the sum over the p_x -, p_y -, and p_z -components.

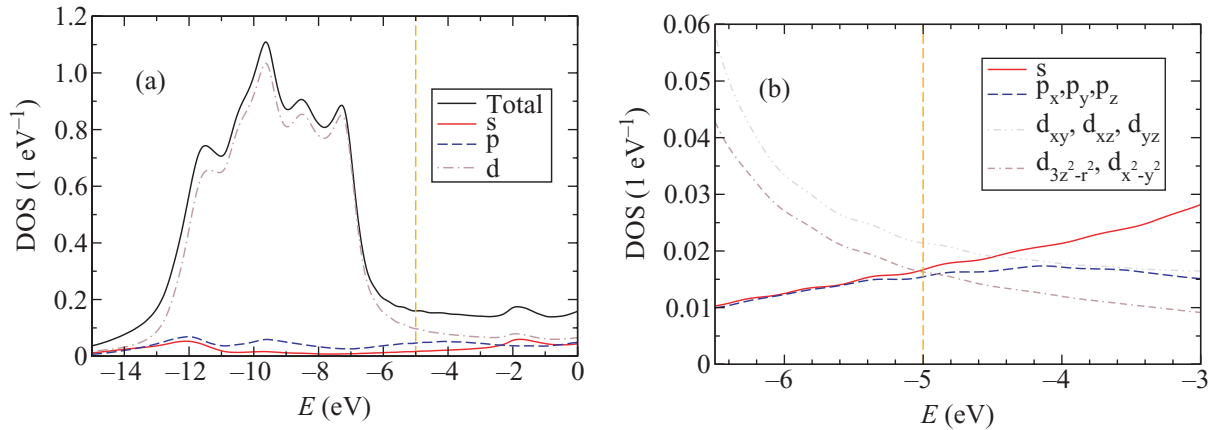


Figure 3. DOS for Au. (a) DOS resolved into s, p and d contributions and (b) into all individual orbital components. The dashed vertical line indicates $E_F = -5.0$ eV.

When an atomic contact of Au is in a dimer or atomic chain configuration, a conductance of around $1G_0$ is expected from experimental measurements [62]–[66] as well as from theoretical studies [7], [67]–[70]. The analysis shows that this value of the conductance is due to a single, almost fully transparent transmission eigenchannel. It arises dominantly from the s orbitals of the noble metal Au, since the electronic structure in the narrowest part of the contact resembles more the electronic configuration of the atom [66, 67].

3.1.1. Determination of contact geometries. Despite the consensus that the conductance of atomic chains of Au is around $1G_0$, the precise atomic positions play an important role [70, 71]. Therefore it is necessary to construct reference geometries that have been studied with a well-established transport method. We choose to compare with results obtained with TRANSIESTA [7]. The ECCs investigated are shown in figure 4. The four-atom Au chain with electrodes oriented in the [100]-direction, called Au100c4, corresponds to a contact geometry examined in [72] (see figure 1(b) therein). The three-atom Au chain, Au111c3, is similar to a configuration in figure 9(d) of [7]. In addition, we study a Au dimer contact, Au111c2, where a two-atom chain is forming the narrowest part. In contrast to Au100c4, for the latter two contacts, the electrodes are along the [111]-direction. In each ECC, the main crystallographic direction is aligned with the z-axis, which is the transport direction.

Let us briefly explain, how we determine these geometries (figure 4). For Au100c4, we construct two ideal, atomically sharp Au [100] pyramids, with two atoms in between. The pyramids end with the layer consisting of 25 atoms. The distance between the layers containing four atoms is set to 12.68 \AA (figure 4(a)), as in [72]. Next, we relax the four-chain atoms without imposing symmetries, keeping all other atoms fixed. After geometry optimization, we find that the configuration agrees well with symmetry D_{4h} . We add two more Au layers with 16 and 9 atoms on each side, where the ECC now consists of 162 atoms, and perform a final DFT calculation, exploiting the symmetry D_{4h} . Compared with [72], all bond distances indicated in figure 4(a) agree within 0.01 \AA , except for the distance between the central chain atoms, where our distance is shorter by 0.07 \AA . For Au111c3, we proceed similarly to Au100c4 (figure 4(b)). We start with two perfect Au [111] pyramids, set the distance between the Au layers with 3

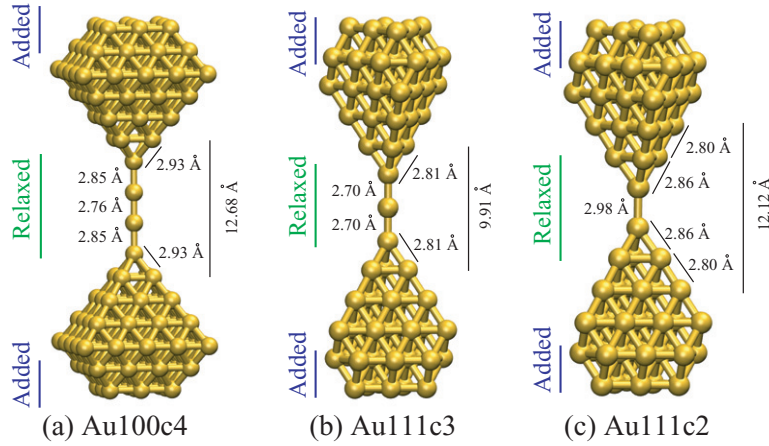


Figure 4. ECCs for Au. (a) Au100c4 is a four-atom chain, (b) Au111c3 is a three-atom chain and (c) Au111c2 is a two-atom chain or dimer contact. For Au100c4, electrodes are oriented in the [100]-direction, whereas for Au111c3 and Au111c2, electrodes are oriented the [111]-direction. Indicated are also the most important bond distances together with information on the construction of the ECCs.

atoms to 9.91 Å [7], and cut the pyramid off at the layers containing 10 atoms. Then we add one atom in the middle, relax the three-chain atoms, add two layers on each side with 12 and 6 atoms, and perform a calculation in symmetry D_{3d} . Au111c3 consists of 77 atoms in total. Our bond distances agree with those in figure 9(d) of [7] to within 0.02 Å. For Au111c2, we include also the first Au layer in the geometry optimization process. The distance between the fixed layers with 6 atoms is 12.12 Å. Otherwise the steps are the same as for Au111c3. The ECC is computed in symmetry D_{3d} and consists of 76 atoms. In the parts excluded from the geometry optimization, atoms are all positioned on the fcc lattice, where we set the lattice constant to the experimental value of 4.08 Å, which corresponds to a nearest-neighbor distance of 2.88 Å.

3.1.2. Four-atom gold chain. Let us now study the conduction properties for the contact Au100c4 (figure 5(a)). There are different possibilities to partition the ECC into the L, C and R regions. The cuts should be done so that L and R are unconnected ($S_{LR} = 0$ and $H_{LR} = 0$, see section 2.2). Hence, the C region must be long enough. In order to describe well the coupling to the electrode surface (figure 1), it is furthermore necessary to have sufficiently many layers in the L and R regions. We observe that at least two of them are needed to obtain reasonable transmission curves. For the two different cuts of the ECC $\tau(E)$ is plotted in figure 5(b). In both cases it is found to be almost identical, indicating the reliability of our method. The transmissions at the Fermi energy are $\tau(E_F) = 0.93$ and 0.98 for cuts 1 and 2, respectively. These values correspond well to the result $\tau(E_F) = 0.99$ of [72].

For cut 2, it is visible in figure 5(c) that the transmission at E_F is dominated by a single eigenchannel, in good agreement with experimental observations [66] and previous theoretical studies [7, 68]. In general, the electronic structure at the narrowest part should have the most decisive influence on the conductance of an atomic contact. Therefore, we plot in figure 5(d) the LDOS of the atom indicated by the arrow in figure 5(a), resolved in its orbital contributions.

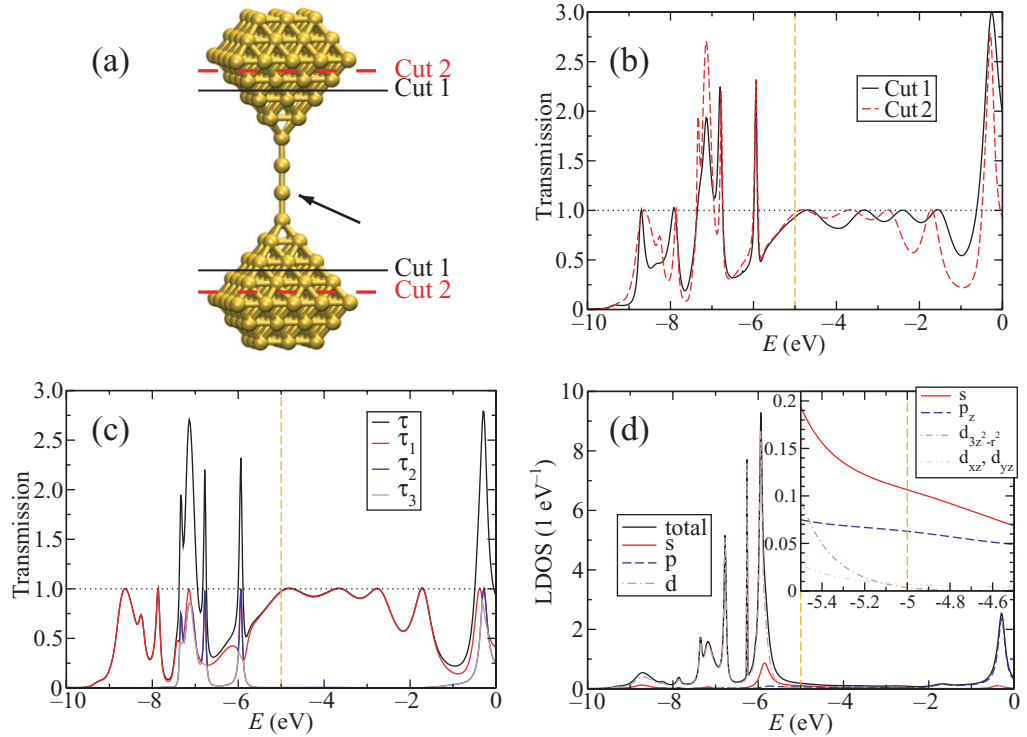


Figure 5. Au100c4. (a) ECC with two different partitionings into L, C and R regions, cuts 1 and 2, and (b) the transmission as a function of the energy for these cuts. For cut 2 (c) transmission resolved into its eigenchannels and (d) LDOS of the chain atom indicated in the ECC with its orbital contributions.

Compared with the DOS of figure 3, it is dominated by s at E_F , where the contributions of all other orbitals than s and p_z are suppressed. These two orbitals form the almost fully transparent transmission eigenchannel, which is rotationally symmetric with respect to the z-axis.

3.1.3. Three-atom gold chain. Exactly the same analysis will now be carried out for the contact Au111c3. In figure 6, the geometry of the ECC, the transmission for different partitionings, the transmission eigenchannels, and the LDOS of the central chain atom are shown. As for Au100c4, we observe that the different cuts yield very similar transmission curves (figure 6(b)). Furthermore all the basic features in $\tau(E)$ are the same as in the TRANSIESTA calculation (see figure 11(d) of [7]). Above the d band, which exhibits a very narrow and high final peak, there is a dip in $\tau(E)$ in both cases. The transmission recovers, however, and a flat region with a value of around 1 is visible. At the Fermi energy cuts 1 and 2 yield $\tau(E_F) = 0.96$ and 0.99 , respectively. This is in reasonable agreement with $\tau(E_F) = 0.94$ in [7], considering the differences in the electrode geometry, basis set, and exchange-correlation functional. We observe from figure 6(c) for cut 1 that the transmission at E_F is dominated by a single eigenchannel, and the LDOS indicates a dominant contribution of s orbitals (figure 6(d)).

3.1.4. Two-atom gold chain. The transmission and LDOS resolved into eigenchannels and orbital components, respectively, are shown in figure 7 for the dimer contact Au111c2. As for Au100c4 and Au111c3, we observe a single dominant eigenchannel at E_F , and $\tau(E_F) = 0.96$.

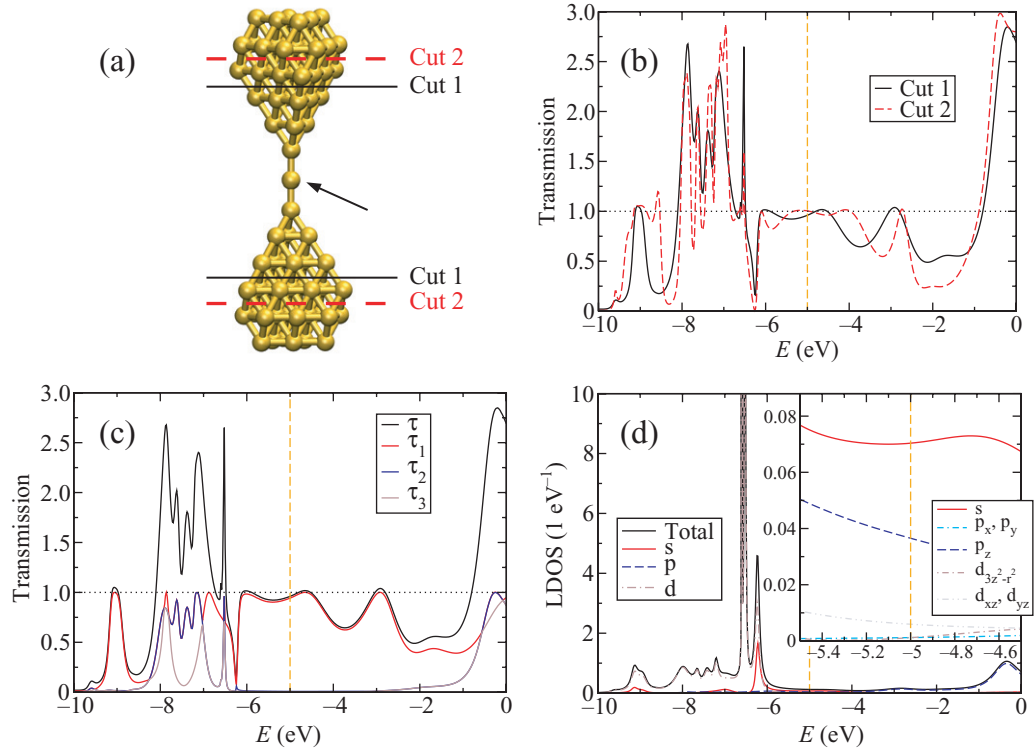


Figure 6. Au111c3. (a) ECC with two different partitionings into L, C and R regions, cuts 1 and 2, and (b) the transmission as a function of the energy for these cuts. For cut 1 (c) transmission resolved into its eigenchannels and (d) LDOS of the central chain atom indicated in the ECC with its orbital contributions.

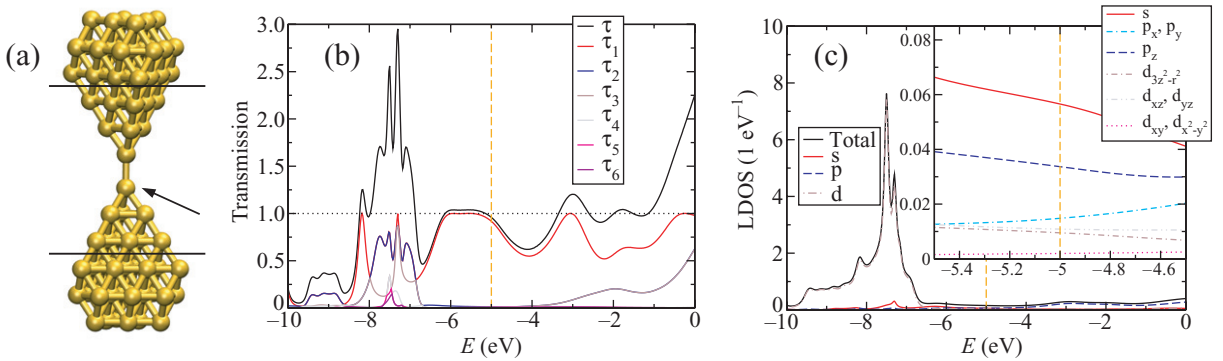


Figure 7. Au111c2. (a) ECC, (b) transmission resolved into its eigenchannels for the cut indicated, and (c) LDOS of the tip atom with its orbital contributions.

The finding of such a dominant channel for chains of two or more atoms is in good agreement with our analysis of less symmetric contacts, which were based on a combination of a tight-binding model and classical molecular dynamics simulations [70]. However, that $\tau(E)$ increases partly even above one in the vicinity of E_F signals that the influence of other channels is increased as compared with Au100c4 and Au111c3. Indeed, the LDOS of the atom in the

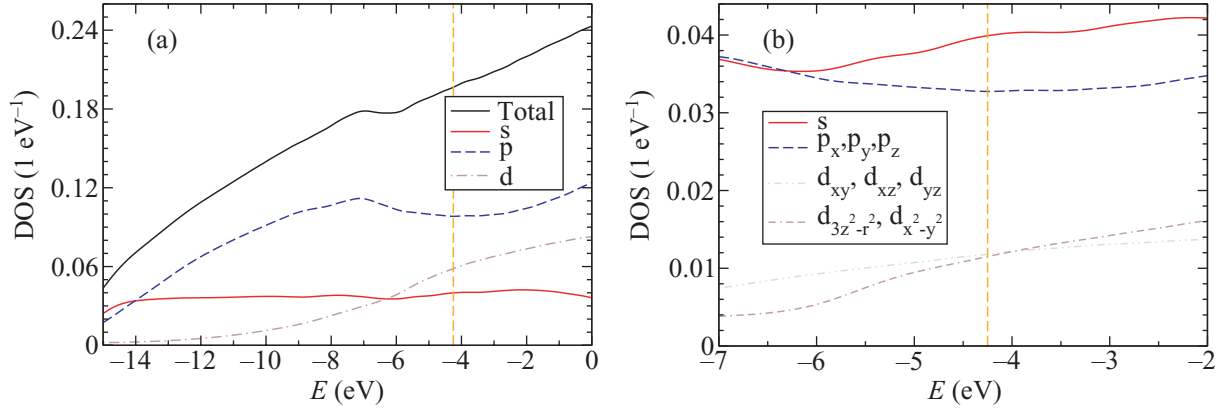


Figure 8. DOS for Al. (a) DOS resolved into s, p and d contributions and (b) into all individual orbital components. The dashed vertical line indicates $E_F = -4.3 \text{ eV}$.

narrowest part of the constriction (figures 7(a) and (c)) shows in particular increased p_x and p_y contributions. Also, the d states exhibit a less pronounced peak structure than was visible in figures 5(d) and 6(d). This is due to the higher coordination number of the atom and the enhanced coupling to the electrodes.

3.2. Aluminium contacts

As is visible from the DOS in figure 8, the electronic structure of Al differs substantially from that of Au. While the latter is a noble metal with an s valence, the Al atom has the electronic configuration $[\text{Ne}] 3s^2 3p^1$ with an open p shell, and the metal is hence considered sp-valent. The strong contribution of s and p states is also observable in the DOS, where d states play only a minor role. As compared with Au, the DOS exhibits a noticeable energy dependence around E_F .

For Al, we study an ideal fcc [111] pyramid, consisting of 251 atoms (figure 9(a)), henceforth referred to as Al111c1. Ideal means that the atoms are positioned on an fcc lattice with the experimental lattice constant $a_0 = 4.05 \text{ \AA}$.

3.2.1. Aluminium single-atom contact. In figure 9, the transmission is displayed for three different partitionings of the ECC Al111c1. Also shown are the transmission eigenchannels and the LDOS of the atom in the narrowest part of the contact for a selected cut. For energies below -6 eV , there are practically no differences visible between the curves for the three different partitionings. Nevertheless, some deviations arise at E_F , and we obtain $\tau(E_F) = 2.36$ (cut 1), 1.88 (cut 2) and 2.23 (cut 3). We attribute these variations to spurious scattering at the LC and CR interfaces, similar to Au. Our values for $\tau(E_F)$ of around 2 agrees nicely with those reported for single-atom contacts in [12]. Compared with Au, the structure of the transmission eigenchannels has changed in an obvious way. There are three channels at E_F , which is in line with experimental observations of Scheer *et al* [66, 73]. Due to the D_{3d} symmetry of the ECC, degeneracies arise, where in particular $\tau_2 = \tau_3$. As is visible from the LDOS, these additional eigenchannel contributions mainly stem from the p_x and p_y orbitals, whereas s and p_z form the nondegenerate first channel [66, 67, 74].

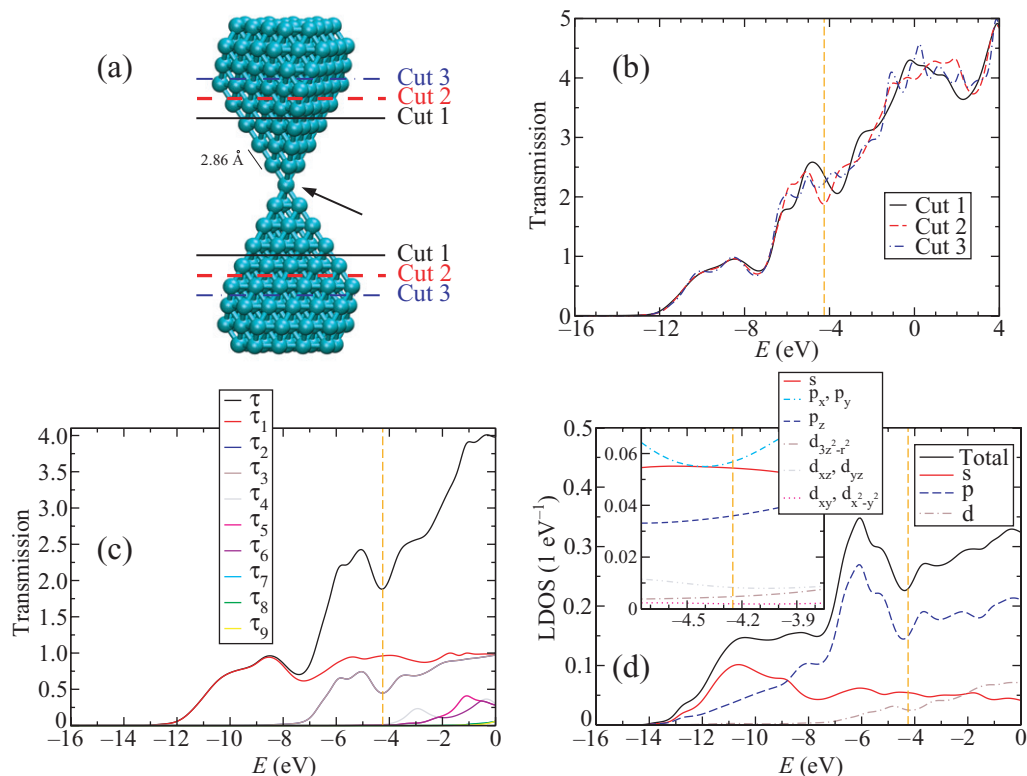


Figure 9. All111c1. (a) ECC with three different partitionings into L, C and R regions, cuts 1, 2 and 3, and (b) the transmission as a function of the energy for these cuts. For cut 2 (c) the transmission resolved into its eigenchannels and (d) the LDOS of the central atom, indicated in the ECC. The nearest-neighbor distance shown in the ECC is identical for all atoms.

4. Conclusions

In conclusion, we have developed a cluster-based method to study the charge transport properties of molecular and atomic contacts. We treat the electronic structure at the level of DFT, and describe transport in terms of the Landauer formalism expressed with standard Green's function techniques. Special emphasis is placed on the modeling of the electrodes and the construction of the associated bulk parameters from spherical metal clusters. We showed that these clusters need to be sufficiently large to produce a reliable description of bulk properties, where a criterion for the extent of the spherical clusters is set by the overlap of the nonorthogonal basis functions. In our studies we crucially rely on the accurate and efficient quantum-chemical treatment of systems consisting of several hundred atoms, made possible by use of the quantum chemistry package TURBOMOLE. Compared with supercell approaches, our method has the advantage that we genuinely describe single-atom or single-molecule contacts.

As an application of our method, we analyzed Au and Al atomic contacts. Studying a four-, a three-, and a two-atom chain with varied electrode lattice orientations for Au, we found a conductance close to $1G_0$, carried by a single transmission channel. Next, we investigated an ideal Al single-atom contact, and found three transmission channels to contribute significantly to the conductance of around $2G_0$. These results are in good agreement with

previous experimental and theoretical investigations. Although we observe some finite-size effects, we have demonstrated both for Au and Al a sufficient robustness of our transmission curves with respect to partitionings of the contact systems. The results illustrate the applicability of our approach to various electrode materials.

Beside the metallic atomic contacts examined here, we have applied the method in the field of molecular electronics. Studies include the dc conduction properties of dithiolated-oligophenylene and diamino-alkane junctions [32], [34]–[36] as well as oxygen adsorbates in Al contacts [33]. In addition, the thermopower [36] and photoconductance [32] of molecular junctions have been investigated in this way. Our studies demonstrate the value of parameter-free modeling for understanding transport at the molecular and atomic scale.

Acknowledgments

We thank R Ahlrichs for providing us with TURBOMOLE and acknowledge stimulating discussions with him and members of his group, in particular N Crawford, F Furche, M Kattannek, P Nava, D Rappoport, C Schrodtr, M Sierka and F Weigend. This work was supported by the Helmholtz Gemeinschaft (contract no VH-NG-029), by the EU network BIMORE (grant no MRTN-CT-2006-035859), and by the DFG within the CFN and SPP 1243. MH acknowledges funding by the Karlsruhe House of Young Scientists and FP that of a Young Investigator Group at KIT.

Appendix A. Nonorthogonal, local basis sets

For practical reasons, one often employs nonorthogonal basis sets in quantum-chemical calculations, consisting for example of a finite set of Gaussian functions. The electronic structure is then described in the spirit of the linear combination of atomic orbitals (LCAO) [41, 75, 76], and this is also how TURBOMOLE is implemented. While it is in principle always possible to transform to an orthogonal basis, it may be more convenient to work directly with the nonorthogonal states.

A concise mathematical description using nonorthogonal basis states can be formulated in terms of tensors. The formalism is presented in a fairly general form in [77], where also aspects of second quantization are addressed. Below, we discuss some of the subtleties related to the use of nonorthogonal basis functions that are important for our method [58]. Since the basis functions are real-valued in our case, the full complexity of the tensor formalism is not needed [78, 79]. Furthermore, we use a simplified notation, where all tensor indices appear as subscripts of matrices.

A.1. Current formula

The most important quantity for transport calculations is the electric current. In the NEGF formalism, its determination requires a separation of the contact into subsystems similar to figure 1(a) [52, 80, 81]. However, due to the overlap of the basis functions in a nonorthogonal basis, the charges of the subsystems are not well defined. Different ways of determining them exist, e.g. the Mulliken or Löwdin population analyses [75]. Despite these additional complications, the Landauer formula (equation (2)) can be derived in a similar fashion as for an orthogonal basis. Recent discussions of the derivation can be found in [51, 82].

A.2. Single-particle Green's functions

Consider the single-particle Hamiltonian H describing the entire system. The retarded Green's operator is defined as $G^r(E) = [(E + i0^+) - H]^{-1}$. Now consider the local, nonorthogonal basis $|i\rangle$ with the matrix elements of the overlap $S_{ij} = \langle i|j\rangle$ and the Hamiltonian $H_{ij} = \langle i|H|j\rangle$. Compared with section 2.2 the index i , used throughout this appendix, is a collective index, denoting both the position at which the basis state is centered and its type. The components of the retarded Green's function, defined by $G^r = \sum_{i,j} |i\rangle G_{ij}^r \langle j|$,¹¹ satisfy the equation [50].

$$\sum_k [(E + i0^+) S_{jk} - H_{jk}] G_{kl}^r(E) = \delta_{jl}. \quad (\text{A.1})$$

The Green's function G_{CC}^r is defined as G_{ij}^r restricted to the central region C. It can be calculated according to equation (5). Due to the nonorthogonal basis the perturbation that couples C to the lead $X = \text{L, R}$ and enters the self-energy (equation (6)) is given by $H_{\text{CX}} - E S_{\text{CX}}$ and thus includes also an overlap contribution. It is interesting to observe that as $E \rightarrow \infty$ the self-energies and the Green's function behave as

$$\Sigma_X^r(E) \xrightarrow{E \rightarrow \infty} E S_{\text{CX}} (S_{\text{XX}})^{-1} S_{\text{XC}}, \quad (\text{A.2})$$

$$G_{\text{CC}}^r \xrightarrow{E \rightarrow \infty} E^{-1} (S^{-1})_{\text{CC}} \quad (\text{A.3})$$

with

$$(S^{-1})_{\text{CC}} = \left[S_{\text{CC}} + \sum_{X=\text{L,R}} S_{\text{CX}} (S_{\text{XX}})^{-1} S_{\text{XC}} \right]^{-1}. \quad (\text{A.4})$$

Equation (A.4) describes the 'renormalization' of the inverse overlap matrix of C due to the coupling to the leads.

A.3. LDOS

We have defined the LDOS at atom i and its decomposition into orbitals α in equations (10) and (11). Let us discuss these definitions further. Consider the energy eigenstates $|\mu\rangle$ of the entire system, satisfying $H|\mu\rangle = \varepsilon_\mu |\mu\rangle$. In this basis, the spectral density of equation (9) has the components $\rho_{\mu\nu}(E) = \langle \mu | \rho(E) | \nu \rangle = \delta(E - \varepsilon_\mu) \delta_{\mu\nu}$. Clearly, they fulfill the normalization

$$\int_{-\infty}^{\infty} dE \rho_{\mu\nu}(E) = \delta_{\mu\nu}. \quad (\text{A.5})$$

If, instead, we consider the components defined by $\rho_{ij}(E) = -\text{Im}[G_{ij}^r(E)]/\pi$, where $G_{ij}^r(E)$ is given by equation (A.1), we find

$$\int_{-\infty}^{\infty} dE \rho_{ij}(E) = (S^{-1})_{ij}. \quad (\text{A.6})$$

Performing a Löwdin orthogonalization of the basis

$$\sum_{k,l} \int_{-\infty}^{\infty} dE (S^{1/2})_{ik} \rho_{kl}(E) (S^{1/2})_{lj} = \delta_{ij}, \quad (\text{A.7})$$

¹¹ Note that the S_{ij} and H_{ij} are the covariant components of the identity and H , respectively, whereas G_{ij}^r are the contravariant components of G^r [78, 79, 85, 86]. In the conventional tensor formulation they would be written $(G^r)^{ij}$, but in our simplified notation no distinction between co- and contravariant components is made.

the normalized LDOS is given as a diagonal element of the integrand. The function $\text{LDOS}_{i\alpha}(E)$ of equation (11) (with $i\alpha \rightarrow i$) is an approximation to this, where all indices are restricted to C. Since $\rho_{\text{CC}}(E) = -\text{Im}[G'_{\text{CC}}(E)]/\pi$ is a positive-semidefinite matrix, it is easy to show that $\text{LDOS}_{i\alpha}(E)$ is positive for all E . However, the normalization $\int_{-\infty}^{\infty} dE \text{LDOS}_{i\alpha}(E) = 1$ is only approximately fulfilled. This could be corrected by multiplying in equation (11) with $(S^{-1})_{\text{CC}}^{-1/2}$ (equation (A.4)) instead of $S_{\text{CC}}^{1/2}$. But since the contributions $\sum_{X=L,R} S_{\text{CX}}(S_{\text{XX}})^{-1} S_{\text{XC}}$ constitute only a surface correction, their neglect may be justified for atoms in the middle of C.

Appendix B. Bulk parameters from finite clusters

B.1. Size requirement for cluster construction

How large do the spherical metal clusters (figure 2) need to be for a convergence of the bulk parameters? Since the matrix elements of the Hamiltonian and the overlap decay similarly with increasing interatomic distance (for exchange–correlation functionals without a contribution of Hartree–Fock exchange), we can concentrate on the overlap. Then, a rather well-defined criterion can be found. The clusters should be so large that the extracted bulk overlap matrix is positive-semidefinite.

We define states $|\vec{k}, \alpha\rangle = \sum_j e^{i\vec{k}\cdot\vec{R}_j} |j, \alpha\rangle$ in k -space. Since $S_{i\alpha,j\beta} = \langle i, \alpha | j, \beta \rangle$ is a positive-semidefinite matrix [75], the same is true for the overlap in k -space

$$\begin{aligned} S_{\alpha\beta}(\vec{k}, \vec{k}') &= \langle \vec{k}, \alpha | \vec{k}', \beta \rangle = \sum_{l,m} e^{-i\vec{k}\cdot\vec{R}_l} S_{l\alpha,m\beta} e^{i\vec{k}'\cdot\vec{R}_m} \\ &= \mathcal{N} \delta_{\vec{k}, \vec{k}'} S_{\alpha\beta}(\vec{k}), \end{aligned} \quad (\text{B.1})$$

where we used that $S_{l\alpha,m\beta} = S_{(l-m)\alpha,0\beta}$. In the expression, \mathcal{N} is the number of atoms in the crystal and

$$S_{\alpha\beta}(\vec{k}) = \sum_j e^{-i\vec{k}\cdot\vec{R}_j} S_{j\alpha,0\beta}. \quad (\text{B.2})$$

In order to study the positive-semidefiniteness of $S_{\alpha\beta}(\vec{k}, \vec{k}')$ it is hence sufficient to investigate the behavior of $S_{\alpha\beta}(\vec{k})$. To do so for a complex quantum-chemistry basis set, we define the positive-definiteness measure

$$\xi(R^{\text{sphere}}) = \min_{\vec{k}} (\mathcal{S}(\vec{k})). \quad (\text{B.3})$$

In this equation, $\mathcal{S}(\vec{k})$ is the smallest eigenvalue of the matrix $S_{\alpha\beta}(\vec{k})$, where $S_{\alpha\beta}(\vec{k})$ is constructed from the bulk parameters extracted from a cluster with radius R^{sphere} [$S_{\alpha\beta}(\vec{k}) = \sum_{\vec{R}_j: |\vec{R}_j| \leq R^{\text{sphere}}} e^{-i\vec{k}\cdot\vec{R}_j} S_{j\alpha,0\beta}$]. In the discrete Fourier transformations (see appendix C.3), we assume periodic boundary conditions with a finite periodicity length along the standard primitive lattice vectors [56, 58]. R^{sphere} must be chosen large enough for ξ to be positive or, if ξ remains negative, it must at least be sufficiently small in absolute value.

Let us first illustrate the behavior of ξ at the example of an s-orbital model. Gaussian s-functions are described by

$$\phi_s(\vec{r}) = \left(\frac{2\gamma}{\pi} \right)^{3/4} e^{-\gamma|\vec{r}|^2} \quad (\text{B.4})$$

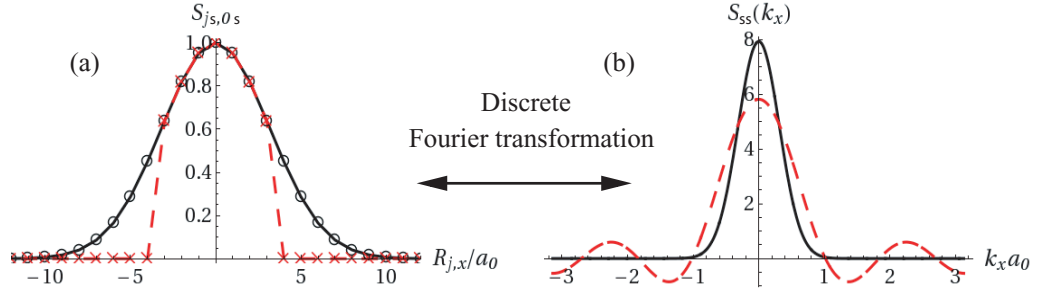


Figure B.1. s-orbital-chain model. (a) The overlap $S_{js,0s}$ of an atom with its neighbors at positions $R_{j,x} = j_1 a_0$ with $j_1 = 0, \pm 1, \dots$ (b) Overlap $S_{ss}(k_x)$ after a discrete Fourier transformation. In both cases, the solid line is for a large cluster and the dashed line for a small cluster.

with an exponent γ , characterizing the radial decay. Hence, the overlap between two atoms

$$S_{js,0s} = \int d^3r \phi_s(\vec{r} - \vec{R}_j) \phi_s(\vec{r}) = e^{-\gamma R_j^2/2} \quad (\text{B.5})$$

decays with their distance $R_j = |\vec{R}_j|$ like a Gaussian function. We consider an infinitely extended chain with atoms at equally spaced positions along the x -axis ($\vec{R}_j = j_1 a_0 \vec{e}_x$). The overlap from a selected atom to its neighbors drops off exponentially (figure B.1(a)). The Fourier transformation will again result in a Gaussian with purely positive values $S_{ss}(k_x)$ (figure B.1(b)). If, however, overlap matrix elements are taken into account only up to a certain maximum value $|\vec{R}_j| \leq R^{\text{sphere}}$, as in a finite cluster, a rough $\sin(k_x)/k_x$ -behavior results, where $S_{ss}(k_x)$ becomes negative at certain k -values. Upon an increase of R^{sphere} , $S_{ss}(k_x)$ will evolve into a Gaussian function and ξ will thus approach zero from below. The negative tails of $S_{ss}(k_x)$ are unphysical, and our observation implies that the clusters used to extract bulk parameters (figure 2) need to be of a sufficiently large radius R^{sphere} , in order to obtain a reliable description of a crystal. Obviously, with our overlap-based criterion the required magnitude of R^{sphere} depends on the basis set chosen.

In figure B.2, we plot the behavior of ξ as a function of R^{sphere} for Au and Al. Beside the results for the SVP basis set, we display ξ for Au also for the basis set LANL2DZ used in [16, 31]. It is visible that ξ is positive for a single atom ($R^{\text{sphere}} = 0$), but negative for small spheres. With increasing R^{sphere} , ξ approaches 0 from below similarly to the s-orbital model. We find that the elimination of diffuse functions reduces the radius R^{sphere} for ξ to become positive or negligibly small. For practical reasons, it may happen that R^{sphere} cannot be chosen large enough. In such a case, negative eigenvalues of $S_{\alpha\beta}(k)$ can lead to negative eigenvalues of the hopping-rate matrices Γ_X (equation (7)), since $\rho_{XX} = -\text{Im}[g_{XX}^r]/\pi$ may no longer be positive-semidefinite (see also the discussion in appendix A.3).

B.2. DOS

The DOS can be used as another measure for the convergence to a solid-state description. With a k -space Hamiltonian in an orthogonal basis set $H^{\text{orth}}(k)$, it is given as

$$\text{DOS}(E) = \sum_{\alpha} \text{DOS}_{\alpha}(E) = -\frac{1}{\pi} \sum_{\alpha} \text{Im} [G_{0\alpha,0\alpha}^{\text{orth},r}(E)]. \quad (\text{B.6})$$

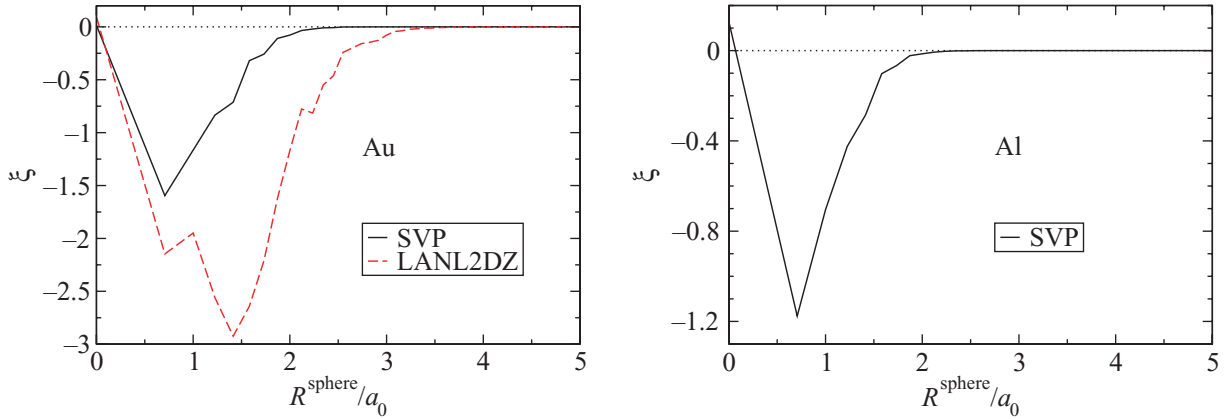


Figure B.2. The positive-definiteness measure ξ for Au and Al as a function of R^{sphere} . Beside the SVP basis set, the behavior of ξ is shown for LANL2DZ used in [16, 31]. $S(\vec{k})$ (equation (B.2)) is evaluated at 32^3 k -points. The radius R^{sphere} has been scaled with the respective lattice constants ($a_0 = 4.08$ Å for Au and $a_0 = 4.05$ Å for Al).

Here, α runs over all basis functions on a bulk atom, and $G_{00}^{\text{orth},r}(E) = \int_{\text{1BZ}} d^3k G^{\text{orth},r}(\vec{k}, E) / V_{\text{1BZ}}$ with the volume V_{1BZ} of the first Brillouin zone (1BZ)¹² and $G^{\text{orth},r}(\vec{k}, E) = [(E + i0^+) - H^{\text{orth}}(\vec{k})]^{-1}$. The orthogonal Hamiltonian can be obtained in several ways. Two possible choices are (i) to Fourier transform S_{j0} and H_{j0} and to perform a Löwdin orthogonalization in k -space $H^{\text{orth}}(\vec{k}) = S^{-1/2}(\vec{k}) H(\vec{k}) S^{-1/2}(\vec{k})$ or (ii) to perform the Löwdin orthogonalization $H^{\text{sphere,orth}} = (S^{-1/2})^{\text{sphere}} H^{\text{sphere}} (S^{-1/2})^{\text{sphere}}$ in real space, to obtain H_{j0}^{orth} by extracting $H_{j0}^{\text{sphere,orth}}$ and by imposing the fcc space group (see also figure 2), and to carry out the Fourier transformation last. For parameters extracted from large enough clusters, we observe the equivalence of the DOS construction with respect to the two different orthogonal Hamiltonians $H^{\text{orth}}(\vec{k})$. If ξ remains (slightly) negative due to a too small R^{sphere} , then the construction of the DOS from the Löwdin orthogonalization in real space (procedure (ii)) is of a higher quality than that resulting from the orthogonalization in k -space (procedure (i)).

In figure B.3 we show the DOS as constructed via procedure (ii) with parameters extracted from different Au and Al spheres with 141 to 555 atoms. We observe that the DOS seems well converged with respect to R^{sphere} both for Au and Al for the largest spherical clusters Au₄₂₉ and Al₅₅₅.

B.3. Transformation of bulk parameters under rotations

We assume that two coordinate systems are connected by the rotation Q , where $\vec{r}' = Q\vec{r}$. The transformation properties of the bulk parameters

$$Y_{j\alpha,0\beta} = \langle j, \alpha | Y | 0, \beta \rangle = \int d^3r \phi_\alpha(\vec{r} - \vec{R}_j) Y(\vec{r}) \phi_\beta(\vec{r})$$

¹² The integration over 1 BZ is implemented as a discrete sum over k -points (see section C.3).

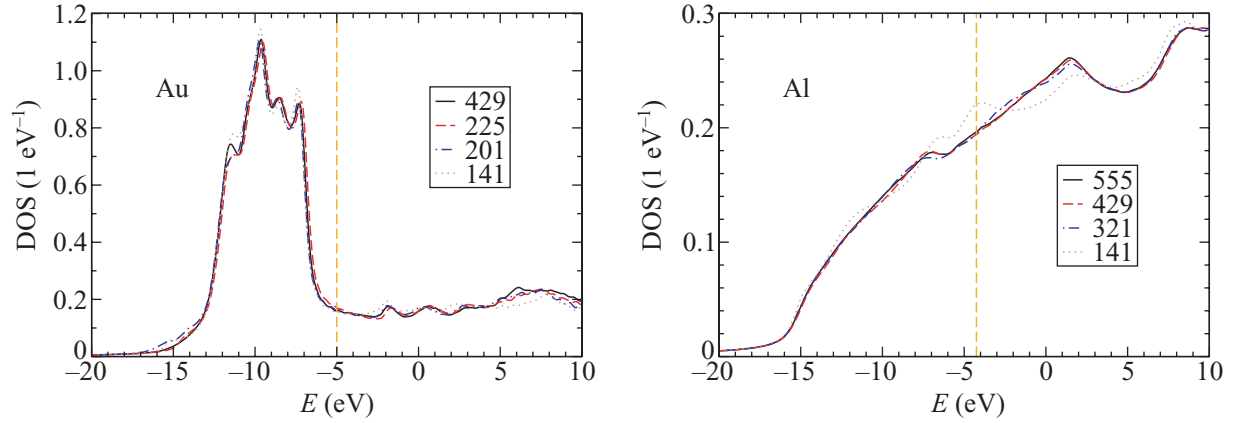


Figure B.3. DOS of Au and Al constructed from parameters extracted from fcc spheres with atom numbers between 141 and 555. The vertical dashed line indicates E_F .

with $Y = S, H$ are determined by those of the basis functions $\langle \vec{r} | j, \alpha \rangle = \phi_\alpha(\vec{r} - \vec{R}_j)$.¹³ The Gaussian basis functions used by TURBOMOLE are characterized by the angular momentum l and the multiplicity $\nu = 1, \dots, 2l+1$, and α is a collective index for both. The rotated basis functions of angular momentum l can be expressed as [83]

$$[\psi']_\nu^l(\vec{r}) = \psi_\nu^l(\varrho^{-1}\vec{r}) = \sum_{\mu=1}^{2l+1} \psi_\mu^l(\vec{r}) D_{\mu\nu}^l(\varrho)$$

with the representation $D_{\mu\nu}^l(\varrho)$ of the rotation ϱ . Using $Y'(\vec{r}) = Y(\varrho^{-1}\vec{r})$, it can be shown that the bulk parameters of the two coordinate systems are related by

$$Y_{\vec{R}_j\alpha, \vec{0}\beta} = \sum_{\mu, \nu} [D^T(\varrho)]_{\alpha\mu} Y'_{\varrho\vec{R}_j\mu, \vec{0}\nu} D(\varrho)_{\nu\beta}, \quad (\text{B.7})$$

where $D(\varrho)$ is the representation of ϱ in the employed basis set. By knowledge of the $D_{\mu\nu}^l(\varrho)$, $D(\varrho)$ can be constructed by the addition of representations [83]. If there are n_l basis functions of angular momentum l in the basis set describing $Y_{j\alpha, 0\beta}$, we have

$$D(\varrho) = \oplus_l n_l D^l(\varrho), \quad (\text{B.8})$$

where \oplus denotes a direct sum.

Let us now give the explicit formulae for the $D^l(\varrho)$. In this work only s, p, and d basis functions are used, and hence we restrict ourselves to $l = 0, 1$ and 2 . Since s functions just depend on the radius, $\psi^0(\vec{r}) = \psi^0(r)$, we have

$$D^0(\varrho) = 1. \quad (\text{B.9})$$

For $l = 1$, there are three p functions, $p_1 = p_x = f_1(r)x$, $p_2 = p_y = f_1(r)y$ and $p_3 = p_z = f_1(r)z$, with a certain radial dependence $f_1(r)$ [76]. Exploiting $\varrho^{-1} = \varrho^T$, we obtain

¹³ We assume that all basis functions are real-valued and that Y is a local single-particle operator $\langle \vec{r} | Y | \vec{r}' \rangle = Y(\vec{r}) \delta(\vec{r} - \vec{r}')$. The identity and Kohn–Sham Fock operator of DFT are of this form.

$p'_i = \sum_{j=1}^3 p_j \varrho_{ji}$. Thus the 3×3 representation of the rotation ϱ for the p functions is

$$D^1(\varrho) = \varrho = \begin{pmatrix} \varrho_{xx} & \varrho_{xy} & \varrho_{xz} \\ \varrho_{yx} & \varrho_{yy} & \varrho_{yz} \\ \varrho_{zx} & \varrho_{zy} & \varrho_{zz} \end{pmatrix}. \quad (\text{B.10})$$

For $l=2$, there are five d functions, where $d_1 = d_{3z^2-r^2} = f_2(r) (3z^2 - r^2) / (2\sqrt{3})$, $d_2 = d_{xz} = f_2(r)xz$, $d_3 = d_{yz} = f_2(r)yz$, $d_4 = d_{xy} = f_2(r)xy$ and $d_5 = d_{x^2-y^2} = f_2(r)(x^2 - y^2)/2$ with some radial dependence $f_2(r)$. The transformed d functions are given as $d'_i = \sum_{j=1}^5 d_j [D^2(\varrho)]_{ji}$ with the 5×5 representation

$$D^2(\varrho) = \begin{pmatrix} (3\varrho_{zz}^2 - 1)/2 & \sqrt{3}\varrho_{zx}\varrho_{zz} & \sqrt{3}\varrho_{zy}\varrho_{zz} & \sqrt{3}\varrho_{zx}\varrho_{zy} & \sqrt{3}(\varrho_{zx}^2 - \varrho_{zy}^2)/2 \\ \sqrt{3}\varrho_{xz}\varrho_{zz} & \varrho_{xx}\varrho_{zz} + \varrho_{zx}\varrho_{xz} & \varrho_{xy}\varrho_{zz} + \varrho_{xz}\varrho_{zy} & \varrho_{xx}\varrho_{zy} + \varrho_{xy}\varrho_{zx} & \varrho_{xx}\varrho_{zx} - \varrho_{xy}\varrho_{zy} \\ \sqrt{3}\varrho_{yz}\varrho_{zz} & \varrho_{yx}\varrho_{zz} + \varrho_{zx}\varrho_{yz} & \varrho_{yy}\varrho_{zz} + \varrho_{yz}\varrho_{zy} & \varrho_{yx}\varrho_{zy} + \varrho_{yy}\varrho_{zx} & \varrho_{yx}\varrho_{zx} - \varrho_{yy}\varrho_{zy} \\ \sqrt{3}\varrho_{xz}\varrho_{yz} & \varrho_{xx}\varrho_{yz} + \varrho_{yx}\varrho_{xz} & \varrho_{xy}\varrho_{yz} + \varrho_{yy}\varrho_{xz} & \varrho_{xx}\varrho_{yy} + \varrho_{xy}\varrho_{yx} & \varrho_{xx}\varrho_{yx} - \varrho_{xy}\varrho_{yy} \\ \sqrt{3}(\varrho_{xz}^2 - \varrho_{yz}^2)/2 & \varrho_{xx}\varrho_{xz} - \varrho_{yx}\varrho_{yz} & \varrho_{xy}\varrho_{xz} - \varrho_{yy}\varrho_{yz} & \varrho_{xx}\varrho_{xy} - \varrho_{yx}\varrho_{yy} & (\varrho_{xx}^2 + \varrho_{yy}^2 - \varrho_{xy}^2 - \varrho_{yx}^2)/2 \end{pmatrix}. \quad (\text{B.11})$$

B.4. Imposing the fcc-space-group symmetry

In this section, we consider how to impose the fcc space group on the parameters $H_{j\alpha,0\beta}^{\text{sphere}}$, extracted from the finite spherical fcc clusters (figure 2). Assuming basis functions to be real-valued, the matrix elements of a translationally invariant Hamiltonian H^{trans} are symmetric and obey the relations

$$H_{i\alpha,j\beta}^{\text{trans}} = H_{(i-j)\alpha,0\beta}^{\text{trans}} = H_{0\alpha,-(i-j)\beta}^{\text{trans}} = H_{-(i-j)\beta,0\alpha}^{\text{trans}}. \quad (\text{B.12})$$

Owing to surface effects, the translational symmetry is not fulfilled for the parameters $H_{j\alpha,0\beta}^{\text{sphere}}$, as illustrated in figure B.4. Hence, although the deviations decrease with growing radius of the spheres, the translational symmetry needs to be enforced in order to describe a crystal. To avoid numerical errors, we impose at the same time the point-group symmetry O_h , although that symmetry is already present due to the shape of our clusters. Concerning the notation, we call the parameters conforming to the O_h point group, the translational symmetry, and the fcc space group $H_{j\alpha,0\beta}^{O_h}$, $H_{j\alpha,0\beta}^{\text{trans}}$, and $H_{j\alpha,0\beta} = H_{j\alpha,0\beta}^{\text{fcc}}$, respectively. We do not need to consider the overlap, since it depends only on the relative position of two atoms.

B.4.1. O_h point group. With equation (B.7) a Hamiltonian $H_{j\alpha,0\beta}^{O_h}$ conforming to the point-group symmetry can be constructed by averaging, for a given element of $H_{j\alpha,0\beta}^{O_h}$, over all $H_{j\alpha,0\beta}^{\text{sphere}}$ related to it by symmetry

$$H_{\vec{R}_j\alpha,\vec{0}\beta}^{O_h} = \frac{1}{N_{O_h}} \sum_{\varrho \in O_h} \sum_{\mu,\nu} [D^T(\varrho)]_{\alpha,\mu} H_{\varrho\vec{R}_j\mu,\vec{0}\nu}^{\text{sphere}} D(\varrho)_{\nu\beta}. \quad (\text{B.13})$$

Here, ϱ runs over all $N_{O_h} = 48$ symmetry operations of the point group O_h [83, 84].

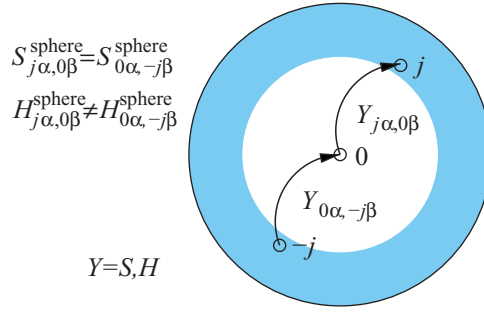


Figure B.4. Necessity to impose the translational symmetry on the hopping elements $H_{j\alpha,0\beta}^{\text{sphere}}$. A finite spherical cluster is displayed. In blue-shaded areas surface effects are important. While the overlap elements $S_{j\alpha,0\beta}^{\text{sphere}}$ are translationally symmetric, this is not the case for $H_{j\alpha,0\beta}^{\text{sphere}}$. In particular $S_{j\alpha,0\beta}^{\text{sphere}} = S_{0\alpha,-j\beta}^{\text{sphere}}$, whereas $H_{j\alpha,0\beta}^{\text{sphere}} \neq H_{0\alpha,-j\beta}^{\text{sphere}}$ as illustrated in the plot.

B.4.2. Translational symmetry. Using equation (B.12), the translational symmetry can be imposed by setting

$$H_{j\alpha,0\beta}^{\text{trans}} = \frac{1}{2} \left(H_{j\alpha,0\beta}^{\text{sphere}} + H_{-j\beta,0\alpha}^{\text{sphere}} \right). \quad (\text{B.14})$$

B.4.3. Fcc space group. The combined action of the O_h point group and the translational symmetry leads to the fcc-space-group symmetry. With equations (B.13) and (B.14) we obtain the parameters $H_{j\alpha,0\beta} = H_{j\alpha,0\beta}^{\text{fcc}}$ according to the prescription

$$H_{\vec{R}_{j\alpha},\vec{0}\beta}^{\text{fcc}} = \frac{1}{2N_{O_h}} \sum_{\varrho \in O_h} \sum_{\mu, \nu} \left\{ [D^T(\varrho)]_{\alpha\mu} H_{\varrho\vec{R}_{j\mu},\vec{0}\nu}^{\text{sphere}} D(\varrho)_{\nu\beta} + [D^T(\varrho)]_{\beta\mu} H_{-\varrho\vec{R}_{j\mu},\vec{0}\nu}^{\text{sphere}} D(\varrho)_{\nu\alpha} \right\}. \quad (\text{B.15})$$

Appendix C. Electrode Green's functions

In this appendix, we describe the last step (figure 2(d)) in the construction of the electrode Green's function g_{XX}^r (equation (6)), which we model as the surface Green's function of a semi-infinite crystal. Since there is a discrete translational invariance in the directions parallel to the surface, the electronic parameters are first Fourier transformed to k -space in these directions. Then the surface Green's function is computed by applying the decimation method of Guinea *et al* [57], generalized to the case of a nonorthogonal basis. Finally, an inverse Fourier transformation is carried out to obtain the Green's function in real space.

C.1. Semi-infinite crystal

The starting point for the construction of the surface Green's functions are the overlap and Hamiltonian elements $S_{j\alpha,0\beta}^{(X)}$ and $H_{j\alpha,0\beta}^{(X)}$ with $X = \text{L, R}$. They have been determined as sketched

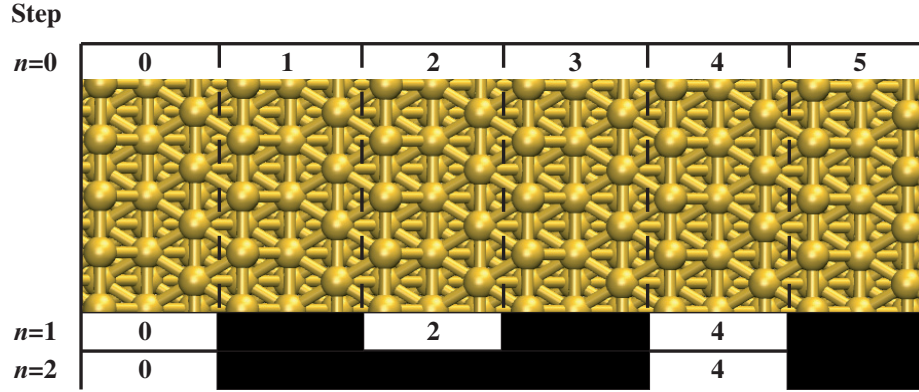


Figure C.1. Au electrode oriented along the [111]-direction. In the illustration, each superlayer consists of $N_3 = 3$ atomic layers. The first six superlayers are displayed with indices running from 0 to 5, as indicated at the top of the figure. In the first step, Green's functions $G_{1,0}^r, G_{3,0}^r, G_{5,0}^r, G_{7,0}^r, \dots$ are eliminated, in the second step Green's functions $G_{2,0}^r, G_{6,0}^r, G_{10,0}^r, G_{14,0}^r, \dots$ and so on. The renormalized couplings $\tau_1^{(n)}$ and $\tau_2^{(n)}$ are effective couplings between superlayers 0 and 2, 2 and 4, and so on for $n = 1$, between 0 and 4, 4 and 8 and so on for $n = 2$, and generally between superlayers with an index difference of 2^n .

in figure 2(a)–(c) and can be used to obtain the overlap and Hamiltonian of the semi-infinite crystal via $S_{m\alpha,m'\beta}^{(X)} = S_{j\alpha,0\beta}^{(X)}$ and $H_{m\alpha,m'\beta}^{(X)} = H_{j\alpha,0\beta}^{(X)}$ with $j = m - m'$. Here, the index tuple $m = (m_1, m_2, m_3)$ refers to the position $\vec{R}_m = \sum_{i=1}^3 m_i \vec{a}_i^{(X)}$ in electrode X with some primitive vectors $\vec{a}_i^{(X)}$. Similar relations hold for m' and j . Note that we restrict the discussion here to Bravais lattices, in particular fcc.

In order to describe the surface of the semi-infinite crystal, e.g. the Au [111] surface¹⁴ displayed in figure C.1, it is convenient to introduce a new set of primitive vectors, which we call $\vec{c}_i^{(X)}$ ($i = 1, 2, 3$). The vectors $\vec{c}_1^{(X)}$ and $\vec{c}_2^{(X)}$ are chosen to span the surface planes, while $\vec{c}_3^{(X)}$ points into the surface. Every lattice point may then be represented also in the new basis as follows: $\vec{R}_m = \sum_{i=1}^2 t_i \vec{c}_i^{(X)} + p \vec{c}_3^{(X)} = \vec{R}_{t,p}$. Hence, the relation $Y_{m\alpha,m'\beta}^{(Xt)} = Y_{tp\alpha,t'p'\beta}^{(X)}$ holds for the electronic parameters with $Y = S, H$. We note that the choice of the $\vec{c}_i^{(X)}$ vectors depends on the orientation of the surface [58] and is not unique, as for any set of primitive vectors. Note also that in our notation the index $t = (t_1, t_2)$ for the transverse direction is a tuple of two integers, while p , numbering the surface planes, is an integer.

Let us now denote with Y any quantity that satisfies the translational symmetry

$$Y_{tp\alpha,t'p'\beta}^{(X)} = Y_{up\alpha,0p'\beta}^{(X)}, \quad u = t - t'. \quad (\text{C.1})$$

Due to the regularity of the semi-infinite crystal, the relation is fulfilled by S and H and therefore also by the surface Green's function g_{XX}^r . The symmetry may be exploited by performing a two-dimensional Fourier transformation with respect to $\vec{r}_u = \sum_{i=1}^2 u_i \vec{c}_i^{(X)}$, resulting in quantities $Y_{p\alpha,p'\beta}^{(X)}(\vec{k}_\lambda)$, where \vec{k}_λ is a vector in k -space. Details on the implementation of the Fourier transformation are discussed further below.

¹⁴ To specify the crystallographic direction, such a [111] in figure C.1, we refer to the vectors of the conventional cubic cell [56].

C.2. Decimation procedure

For the calculation of the lead self-energy for side $X = L, R$ (equation (6)), Green's function g_{XX}^r is needed only for the first few atomic layers of the surface, since the coupling elements $H_{CX} - E S_{CX}$ have a finite range. Therefore, the semi-infinite crystal is divided into superlayers, each consisting of an equal number N_3 of atomic layers (figure C.1). The surface superlayer is given the index 0, and the number N_3 is determined by requiring the hopping elements to be finite only between the nearest-neighbor superlayers and between C and superlayer 0.

We assume from now on that the two-dimensional Fourier transformation to k -space has been performed for all quantities. For notational simplicity, we will suppress the dependence on \vec{k}_λ and on the index (X). Furthermore, the atomic layer indices p, p' and the atomic orbital (or basis function) indices α, β are replaced by superlayer indices m, m' , thus

$$Y_{p\alpha, p'\beta}^{(X)}(\vec{k}_\lambda) \rightarrow Y_{m, m'}. \quad (\text{C.2})$$

If there are M basis functions on each electrode atom, then the element $Y_{m, m'}$ is a matrix block with dimensions $MN_3 \times MN_3$.

In terms of the block matrices, Green's function (equation (A.1)) satisfies

$$\sum_{n=0}^{\infty} [E^+ S_{m, n} - H_{m, n}] G_{n, l}^r = 1_{m, l}, \quad m, l \geq 0, \quad (\text{C.3})$$

where $E^+ = E + i\eta$ with an infinitesimal broadening $\eta > 0$. Within this set of equations, we need to solve for $G_{0,0}^r$. Furthermore, since we are assuming an ideal semi-infinite crystal where $S_{m, m'} = S_{m-m', 0}$ and $H_{m, m'} = H_{m-m', 0}$ with $m, m' \geq 0$, and because $S_{m, 0} = H_{m, 0} = 0$ if $|m| \geq 2$, the set may be simplified to

$$W G_{0,0}^r + \tau_1 G_{1,0}^r = 1, \quad (\text{C.4})$$

$$\tau_2 G_{m-1,0}^r + W G_{m,0}^r + \tau_1 G_{m+1,0}^r = 0, \quad \text{for } m \geq 1, \quad (\text{C.5})$$

where $W = E^+ S_{0,0} - H_{0,0}$, $\tau_1 = E^+ S_{0,1} - H_{0,1}$, $\tau_2 = E^+ S_{1,0} - H_{1,0}$ and $S_{0,0} = S_{0,0}^\dagger$, $H_{0,0} = H_{0,0}^\dagger$, $S_{1,0} = S_{0,1}^\dagger$, $H_{1,0} = H_{0,1}^\dagger$. Note that due to the imaginary part of E^+ , τ_1 and τ_2 are not the Hermitian conjugates of each other. In order to solve equations (C.4) and (C.5) for $G_{0,0}^r$, we now use the iterative decimation scheme [57], illustrated in figure C.1. In the n th step of the iteration, this procedure eliminates all Green's functions $G_{2^{n-1}(2j-1), 0}^r$ with $j \in \mathbb{N} \setminus \{0\}$. The remaining components are then determined through new effective 'onsite' and 'hopping' blocks, given by

$$W_s^{(n)} = W_s^{(n-1)} - \tau_1^{(n-1)} \left(W_b^{(n-1)} \right)^{-1} \tau_2^{(n-1)}, \quad (\text{C.6})$$

$$W_b^{(n)} = W_b^{(n-1)} - \tau_1^{(n-1)} \left(W_b^{(n-1)} \right)^{-1} \tau_2^{(n-1)} - \tau_2^{(n-1)} \left(W_b^{(n-1)} \right)^{-1} \tau_1^{(n-1)}, \quad (\text{C.7})$$

$$\tau_1^{(n)} = -\tau_1^{(n-1)} \left(W_b^{(n-1)} \right)^{-1} \tau_1^{(n-1)}, \quad (\text{C.8})$$

$$\tau_2^{(n)} = -\tau_2^{(n-1)} \left(W_b^{(n-1)} \right)^{-1} \tau_2^{(n-1)}, \quad (\text{C.9})$$

where the matrices of the 0th step are $W_b^{(0)} = W_s^{(0)} = W$, $\tau_1^{(0)} = \tau_1$, and $\tau_2^{(0)} = \tau_2$. In the iterative procedure, the couplings $\tau_1^{(n)}$ and $\tau_2^{(n)}$ describe effective couplings between superlayers with an

index difference of 2^n after n steps (figure C.1). Therefore, the couplings $\tau_1^{(n)}$ and $\tau_2^{(n)}$ can be expected to decrease rapidly as a function of n . If $\tau_1^{(n)}$ and $\tau_2^{(n)}$ are negligible after $n = \nu$ steps, we find

$$G_{0,0}^r = (W_s^{(\nu)})^{-1}. \quad (\text{C.10})$$

Returning to the original notation, the surface Green's function is given by

$$(g_{XX}^r)_{p\alpha,p'\beta}(\vec{k}_\lambda) = (G_{0,0}^r)_{p\alpha,p'\beta}(\vec{k}_\lambda) = \left[(W_s^{(\nu)})^{-1} \right]_{p\alpha,p'\beta}(\vec{k}_\lambda). \quad (\text{C.11})$$

By using an inverse Fourier transformation, we obtain g_{XX}^r in real space (see section C.3)¹⁵.

C.3. Discrete Fourier transformation and further numerical details

For the practical implementation of the two-dimensional Fourier transformations, we assume periodic ('Born-von-Kármán') boundary conditions with a finite periodicity of N_i steps along the vectors $\vec{c}_i^{(X)}$ for $i = 1, 2$ [56]. For any quantity with the symmetry of equation (C.1), the discrete Fourier transformation and its inverse are given as

$$Y_{p\alpha,p'\beta}^{(X)}(\vec{k}_\lambda) = \sum_u Y_{up\alpha,0p'\beta}^{(X)} e^{-i\vec{k}_\lambda \cdot \vec{r}_u}, \quad (\text{C.12})$$

$$Y_{up\alpha,0p'\beta}^{(X)} = \frac{1}{N} \sum_\lambda Y_{p\alpha,p'\beta}^{(X)}(\vec{k}_\lambda) e^{i\vec{k}_\lambda \cdot \vec{r}_u}. \quad (\text{C.13})$$

Here, $\vec{r}_u = \sum_{i=1}^2 u_i \vec{c}_i^{(X)}$, $\vec{k}_\lambda = \sum_{i=1}^2 \lambda_i \vec{d}_i^{(X)}$ and $N = \prod_{i=1}^2 N_i$. The $\vec{d}_i^{(X)}$ are the reciprocal lattice vectors corresponding to the $\vec{c}_i^{(X)}$, and the integer indices u_i and λ_i in the index tuples $u = (u_1, u_2)$ and $\lambda = (\lambda_1, \lambda_2)$ are restricted to the set $M_i = \{-N_i/2, \dots, N_i/2 - 1\}$, where N_i is assumed to be even. The discrete Fourier transformations can be carried out efficiently by employing fast-Fourier-transform algorithms.

Let us assume that the surface Green's function $(g_{XX}^r)_{p\alpha,p'\beta}(\vec{k}_\lambda)$ has been determined in k -space with the help of the decimation (equation (C.11)). Then the matrix elements of g_{XX}^r are constructed via $(g_{XX}^r)_{tp\alpha,t'p'\beta} = (g_{XX}^r)_{up\alpha,0p'\beta}$, where $(g_{XX}^r)_{up\alpha,0p'\beta}$ is obtained from equation (C.13) and $u = t - t'$. For this assignment to yield sensible results, the periods N_1 and N_2 in the Fourier transformations need to be chosen large enough to fulfill two conditions. Firstly, the bulk parameters $S_{up\alpha,0p'\beta}^{(X)}$ and $H_{up\alpha,0p'\beta}^{(X)}$ should have decayed to negligible values for u at the borders of the area $M_1 \times M_2$. Secondly, all u occurring in the assignment must be contained in $M_1 \times M_2$.

In our calculations we used periodicity lengths $N_1 = N_2 = 32$, corresponding to $N = 32^2$ k -points. The broadening parameter for the electrode Green's function was chosen such that we obtain a reasonably smooth DOS, which does not change much for an increased number N of k -points (section B.2). We observe that there exists a certain balance between the broadening η and N : the larger the N , the smaller can η be [58]. We employed $\eta = 10^{-2}$ H for Au and $\eta = 2 \times 10^{-2}$ H for Al.

The decimation procedure is formally the same for the L and R electrodes, and needs to be carried out separately for them in general. However, computer time can be saved, for example,

¹⁵ We note that the decimation also provides the Green's function $G_{m,m}^r = (W_b^{(\nu)})^{-1}$ for a bulk superlayer with $m \geq 2^\nu$.

by choosing both electrodes along the same crystallographic direction and by orienting them in the same way. In such a case, the vectors $\vec{c}_i^{(X)}$ are identical for $X = \text{L, R}$. Consequently, W , τ_1 , and τ_2 need to be constructed only once, and the decimation can be done simultaneously for both sides. For the convergence criterion, we use

$$\sum_{i,j} \left| \left[\tau_1^{(n-1)} \left(W_b^{(n-1)} \right)^{-1} \tau_2^{(n-1)} \right]_{i,j} \right| < \varepsilon.$$

In this way, we have a direct control on how much the inverse surface Green's function (equation (C.6)) is still modified. Here, $\varepsilon = 10^{-6}$ H turned out to be sufficient to converge the transmission curves.

References

- [1] Nitzan A and Ratner M A 2003 *Science* **300** 1384
- [2] Nazin G V, Qiu X H and Ho W 2003 *Science* **302** 77
- [3] Tao N J 2006 *Nat. Nanotechnol.* **1** 173
- [4] Lindsay S M and Ratner M A 2007 *Adv. Mater.* **19** 23
- [5] Akkerman H B and de Boer B 2008 *J. Phys.: Condens. Matter* **20** 013001
- [6] Agrat N, Yeyati A L and van Ruitenbeek J M 2003 *Phys. Rep.* **377** 81
- [7] Brandbyge M, Mozos J-L, Ordejón P, Taylor J and Stokbro K 2002 *Phys. Rev. B* **65** 165401
- [8] Palacios J J, Pérez-Jiménez A J, Louis E, San-Fabián E and Vergés J. A. 2002 *Phys. Rev. B* **66** 035322
- [9] Xue Y, Datta S and Ratner M A 2001 *J. Chem. Phys.* **115** 4292
- [10] Taylor J, Guo H and Wang J 2001 *Phys. Rev. B* **63** 245407
- [11] Fujimoto Y and Hirose K 2003 *Phys. Rev. B* **67** 195315
- [12] Jelínek P, Pérez R, Ortega J and Flores F 2003 *Phys. Rev. B* **68** 085403
- [13] Havu P, Havu V, Puska M J and Nieminen R M 2004 *Phys. Rev. B* **69** 115325
- [14] Tada T, Kondo M and Yoshizawa K 2004 *J. Chem. Phys.* **121** 8050
- [15] Thygesen K S and Jacobsen K W 2005 *Chem. Phys.* **319** 111
- [16] Damle P S, Gosh A W and Datta S 2001 *Phys. Rev. B* **64** 201403
- [17] Wortmann D, Ishida H and Blügel S 2002 *Phys. Rev. B* **65** 165103
- [18] Evers F, Weigend F and Koentopp M 2004 *Phys. Rev. B* **69** 235411
- [19] Khomyakov P A and Brocks G 2004 *Phys. Rev. B* **70** 195402
- [20] Calzolari A, Marzari N, Souza I and Buongiorno Nardelli M 2004 *Phys. Rev. B* **69** 035108
- [21] Heurich J, Cuevas J C, Wenzel W and Schön G 2002 *Phys. Rev. Lett.* **88** 256803
- [22] Rocha A R, García-Suárez V M, Bailey S, Lambert C, Ferrer J and Sanvito S 2006 *Phys. Rev. B* **73** 085414
- [23] Ferretti A, Calzolari A, Di Felice R, Manghi F, Caldas M J, Buongiorno Nardelli M and Molinari E 2005 *Phys. Rev. Lett.* **94** 116802
- [24] Toher C, Filippetti A, Sanvito S and Burke K 2005 *Phys. Rev. Lett.* **95** 146402
- [25] Darancet P, Ferretti A, Mayou D and Olevano V 2007 *Phys. Rev. B* **75** 075102
- [26] Thygesen K S and Rubio A 2008 *Phys. Rev. B* **77** 115333
- [27] Cuevas J C, Heurich J, Pauly F, Wenzel W and Schön G 2003 *Nanotechnology* **14** R29
- [28] Pecchia A and Di Carlo A 2004 *Rep. Prog. Phys.* **67** 1497
- [29] Koentopp M, Chang C, Burke K and Car R 2008 *J. Phys.: Condens. Matter* **20** 083203
- [30] Papaconstantopoulos D A 1986 *Handbook of the Band Structure of Elemental Solids* (New York: Plenum)
- [31] Damle P, Gosh A W and Datta S 2002 *Chem. Phys.* **281** 171
- [32] Viljas J K, Pauly F and Cuevas J C 2007 *Phys. Rev. B* **76** 033403
- [33] Wohlthat S, Pauly F, Viljas J K, Cuevas J C and Schön G 2007 *Phys. Rev. B* **76** 075413
- [34] Wohlthat S, Pauly F and Reimers J R 2008 *Chem. Phys. Lett.* **454** 284

- [35] Pauly F, Viljas J K, Cuevas J C and Schön G 2008 *Phys. Rev. B* **77** 155312
- [36] Pauly F, Viljas J and Cuevas J 2008 *Phys. Rev. B* **78** 035315
- [37] Ahlrichs R, Bär M, Häser M, Horn H and Kölmel C 1989 *Chem. Phys. Lett.* **162** 165
- [38] Eichkorn K, Treutler O, Öhm H, Häser M and Ahlrichs R 1995 *Chem. Phys. Lett.* **242** 652
- [39] Eichkorn K, Weigend F, Treutler O and Ahlrichs R 1997 *Theor. Chem. Acc.* **97** 119
- [40] Sierka M, Hogeekamp A and Ahlrichs R 2003 *J. Chem. Phys.* **118** 9136
- [41] Koch W and Holthausen M C 2001 *A Chemist's Guide to Density Functional Theory* (Weinheim: Wiley-VCH)
- [42] Fiolhais C, Nogueira F and Marques M (ed) 2003 *A Primer in Density Functional Theory* (Berlin: Springer)
- [43] Becke A D 1988 *Phys. Rev. A* **38** 3098
- [44] Perdew J P 1986 *Phys. Rev. B* **33** 8822
- [45] Ahlrichs R and Elliott S D 1999 *Phys. Chem. Chem. Phys.* **1** 13
- [46] Furche F, Ahlrichs R, Weis P, Jacob C, Gilb S, Bierweiler T and Kappes M M 2002 *J. Chem. Phys.* **117** 6982
- [47] Köhn A, Weigend F and Ahlrichs R 2001 *Phys. Chem. Chem. Phys.* **3** 711
- [48] Nava P, Sierka M and Ahlrichs R 2003 *Phys. Chem. Chem. Phys.* **5** 3372
- [49] Schäfer A, Horn H and Ahlrichs R 1992 *J. Chem. Phys.* **97** 2571
- [50] Xue Y, Datta S and Ratner M A 2002 *Chem. Phys.* **281** 151
- [51] Viljas J K, Cuevas J C, Pauly F and Häfner M 2005 *Phys. Rev. B* **72** 245415
- [52] Datta S 2005 *Electronic Transport in Mesoscopic Systems* (Cambridge: Cambridge University Press)
- [53] Viljas J K, Pauly F and Cuevas J C 2008 *Phys. Rev. B* **77** 155119
- [54] Viljas J K and Cuevas J C 2007 *Phys. Rev. B* **75** 075406
- [55] Economou E N (ed) 2006 *Green's Functions in Quantum Physics* (Berlin: Springer)
- [56] Ashcroft N W and Mermin N D 1976 *Solid State Physics* (Orlando: Harcourt)
- [57] Guinea F, Tejedor C, Flores F and Louis E 1983 *Phys. Rev. B* **28** 4397
- [58] Pauly F 2007 *PhD Thesis* Universität Karlsruhe
- [59] Lide D R 1998 *CRC Handbook of Chemistry and Physics* (Boca Raton, FL: CRC Press)
- [60] Heyd J and Scuseria G E 2003 *J. Chem. Phys.* **118** 8207
- [61] Smit R H M, Untiedt C, Yanson A I and van Ruitenbeek J M 2001 *Phys. Rev. Lett.* **87** 266102
- [62] Ludoph B and van Ruitenbeek J M 2000 *Phys. Rev. B* **61** 2273
- [63] Yanson A I 2001 *PhD Thesis* Universiteit Leiden
- [64] Yanson I K, Shklyarevskii O I, Csonka S, van Kempen H, Speller S, Yanson A I and van Ruitenbeek J M 2005 *Phys. Rev. Lett.* **95** 256806
- [65] Thijssen W H A, Marjenburgh D, Bremmer R H and van Ruitenbeek J M 2006 *Phys. Rev. Lett.* **96** 026806
- [66] Scheer E, Agrät N, Cuevas J C, Yeyati A L, Ludoph B, Martín-Rodero A, Bollinger G R, van Ruitenbeek J M and Urbina C 1998 *Nature* **394** 154
- [67] Cuevas J C, Yeyati A L, Martín-Rodero A, Bollinger G R, Untiedt C and Agrät N 1998 *Phys. Rev. Lett.* **81** 2990
- [68] Mozos J L, Ordejón P, Brandbyge M, Taylor J and Stokbro K 2002 *Nanotechnology* **13** 346
- [69] Lee Y J, Brandbyge M, Puska M J, Taylor J, Stokbro K and Nieminen R M 2004 *Phys. Rev. B* **69** 125409
- [70] Dreher M, Pauly F, Heurich J, Cuevas J C, Scheer E and Nielaba P 2005 *Phys. Rev. B* **72** 075435
- [71] Yanson A I, Rubio-Bolinger G, van den Brom H E, Agrät N and van Ruitenbeek J M 1998 *Nature* **395** 783
- [72] Frederiksen T, Brandbyge M, Lorente N and Jauho A-P 2004 *Phys. Rev. Lett.* **93** 256601
- [73] Scheer E, Joyez P, Esteve D, Urbina C and Devoret M H 1997 *Phys. Rev. Lett.* **78** 3535
- [74] Pauly F, Dreher M, Viljas J K, Häfner M, Cuevas J C and Nielaba P 2006 *Phys. Rev. B* **74** 235106
- [75] Szabo A and Ostlund N S 1996 *Modern Quantum Chemistry: Introduction to Advanced Electronic Structure Theory* (New York: Dover)
- [76] Atkins P and Friedman R 2005 *Molecular Quantum Mechanics* (Oxford: Oxford University Press)
- [77] Artacho E and del Bosch L M 1991 *Phys. Rev. A* **43** 5770
- [78] Iben H K 1999 *Tensorrechnung* (Stuttgart: Teubner)

- [79] Borisenko A I and Tarapov I E 1979 *Vector and Tensor Analysis with Applications* (New York: Dover)
- [80] Caroli C, Combescot R, Nozieres P and Saint-James D 1971 *J. Phys. C: Solid State Phys.* **4** 916
- [81] Meir Y and Wingreen N S 1992 *Phys. Rev. Lett.* **68** 2512
- [82] Thygesen K S 2006 *Phys. Rev. B* **73** 035309
- [83] Hamermesh M 1989 *Group Theory and its Applications to Physical Problems* (New York: Dover)
- [84] Corso A D 1996 *Quantum Mechanical ab initio Calculation of the Properties of Crystalline Materials* ed C Pisani (Berlin: Springer) p 77
- [85] Lohez D and Lannoo M 1983 *Phys. Rev. B* **27** 5007
- [86] Sulston K W and Davison S G 2003 *Phys. Rev. B* **67** 195326